Contemporary Mathematics
https://ojs.wiserpub.com/index.php/CM/

Research Article

Dynamics and Control of a Nine-Mode Reduced-Order Model of the 2D Navier-Stokes Equations

Nejib Smaoui[1]*, Noor El-Ulabi[1], Mohamed Zribi[2]

[1] Department of Mathematics, Faculty of Science, Kuwait University, P.O. Box 5969, Safat, 13060, Kuwait
[2] Department of Electrical Engineering, Faculty of Engineering & Petroleum, Kuwait University, P.O. Box 5969, Safat, 13060, Kuwait
E-mail: n.smaoui@ku.edu.kw, nsmaoui64@yahoo.com

Received: 9 July 2025; **Revised:** 5 August 2025; **Accepted:** 12 August 2025

Abstract: This paper investigates the dynamics and control of the two-Dimensional (2D) Kolmogorov flow, a canonical model in fluid dynamics governed by the 2D incompressible Navier-Stokes equations with periodic boundary conditions and a sinusoidal external forcing in the x-direction. To study this system, a Fourier-Galerkin spectral method is used to derive a reduced-order model consisting of nine nonlinear Ordinary Differential Equations (ODEs) that capture the essential features of the Kolmogorov flow. Compared to an earlier model, the addition of two extra modes allows the new system to exhibit dynamical features such as hysteresis and more intricate bifurcation patterns, which were not captured in previous formulations. The resulting ninth-order ODE system is analyzed in detail to explore its rich dynamical behavior and underlying symmetries across a range of Reynolds numbers $0 < R_e < 30$. Numerical simulations demonstrate the model's ability to reproduce diverse dynamical regimes, including steady states, periodic orbits, and chaotic attractors, confirming the fidelity of the reduced-order representation. Moreover, a Lyapunov-based feedback control strategy is formulated to regulate the system and stabilize it toward desired invariant sets, such as equilibria, periodic trajectories, or chaotic attractors. Numerical experiments are conducted to validate the effectiveness of the proposed control scheme. These findings contribute to broader understanding of nonlinear flow dynamics and control in reduced-order settings and may inform future developments in flow regulation and turbulence management.

***Keywords*:** 2D Navier-Stokes equations, Fourier Galerkin projection, Lyapunov-based control, chaotic attractors

MSC: 34D06, 34H10, 35Q30, 37D45, 37N35

Abbreviation

$\boldsymbol{u}$	Velocity field
p	Pressure field
$\boldsymbol{f}$	External forcing
R_e	Reynolds number
R_{e_1}, R_{e_2}	Reynolds numbers of the master and slave systems, respectively

DOI: https://doi.org/10.37256/cm.6520257774

ν	Kinematic viscosity, defined as $\nu = \frac{1}{R_e}$
$\mathbf{k}$	Wave vector with integer components
$f_{\mathbf{k}}$	Forcing component in Fourier space
$f(x)$	Nonlinear vector function of the reduced system
x_i	State variables of the master system $(i = 1, \ldots, 9)$
x_d	Constant desired fixed point
y_i	State variables of the slave system $(i = 1, \ldots, 9)$
u_i	Control inputs $(i = 1, \ldots, 4)$
ξ_i	Error state between master and slave system variables $(i = 1, \ldots, 9)$
$\mathbf{e}$	Synchronization error vector
b_i	Positive scalar weights in Lyapunov function $(i = 1, \ldots, 9)$
g_i	Controller gain $(i = 1, \ldots, 4)$
V	Lyapunov function candidate
r_x	Reflection symmetry across the x-axis
r_y	Reflection symmetry across the y-axis
r_o	Reflection symmetry across the origin

1. Introduction

The transition from laminar flow to turbulence in incompressible fluids has long been a central topic in fluid dynamics. A prominent approach to studying this transition involves constructing reduced-order models derived from the two-Dimensional (2D) Navier-Stokes equations, also known as the 2D Kolmogorov flow, a fundamental model for investigating instabilities, bifurcation structures, and the transition to turbulence [1]. These low-dimensional models aim to capture the essential features of the system's long-time behavior while significantly reducing computational complexity.

In recent years, substantial efforts have focused on constructing reduced dynamical systems that capture the essential behavior of fluid flows [2–21]. A widely used approach for this purpose is the Fourier-Galerkin method. This technique projects the 2D Navier-Stokes equations onto a finite-dimensional subspace, resulting in systems of Ordinary Differential Equations (ODEs) that approximate the dynamics. Many reduced-order models have been developed using this method, particularly for the case where external forcing is limited to a single Fourier mode [7–20].

Over the past few decades, extensive numerical studies have examined the behavior of Kolmogorov flows under various forcing scenarios. A notable contribution by Boldrighini and Franceschini [8] introduced a five-mode truncation with forcing applied to the $(2, -1)$ Fourier mode. Their work demonstrated a classical bifurcation sequence, progressing from steady states to time-periodic orbits, then to strange attractors, and ultimately to chaotic dynamics as the Reynolds number increased. This model was later extended by Franceschini and Tebaldi [13], who observed an infinite cascade of period-doubling bifurcations and the onset of hysteresis. Their results provided evidence for links to Feigenbaum's universality theory. In 1981, Franceschini and Tebaldi [12] developed a seven-mode truncation, revealing an even richer bifurcation structure and demonstrating the increased complexity that arises with higher-dimensional models. These early studies established a foundation for exploring turbulence onset using low-dimensional models.

In parallel, alternative approaches sought to capture the essential dynamics through data-driven basis expansions. In 1996, Armbruster et al. [7] analyzed Kolmogorov flow forced on mode (0, 2) using symmetry analysis and the Karhunen-Loève (K-L) decomposition, revealing complex bifurcation structures and gluing bifurcations. Smaoui and Armbruster [14] later used K-L decomposition with symmetries to derive a reduced-order 12-mode ODE system. This model replicated the dynamics at moderate Reynolds numbers with good accuracy, though some complex behaviors, such as homoclinic transitions, were not fully captured.

Several studies continued to refine reduced-order modeling. Feudel and Seehafer [6] characterized bifurcation cascades in forced flows. Chen and Price [10] explored Hopf bifurcations leading to stable periodic orbits using low-dimensional truncations. Braun et al. [9] examined the role of boundary conditions in determining the route to

chaos, highlighting differences between period-doubling and torus breakdown scenarios. Nicolis and Nicolis [22] linked dynamical transitions to thermodynamic quantities such as entropy production, providing a bridge between bifurcation theory and nonequilibrium thermodynamics.

More recently, Smaoui [15] proposed a new reduced-order model derived using a direct Fourier-Galerkin approach. He formulated a seventh-order ODE system that approximates the 2D Kolmogorov flow forced on mode (0, 2). This model captured a homoclinic gluing bifurcation similar to that observed by Armbruster et al. [7]. Numerical simulations demonstrated that the system accurately reproduced multiple dynamical regimes, including steady states, periodic orbits, and chaotic behavior. Furthermore, Smaoui proposed two Lyapunov-based control schemes: one to drive the system to a fixed point, and another to synchronize two reduced-order systems with different Reynolds numbers and initial conditions. Building on this, Smaoui et al. [16] analyzed the same model at different Reynolds numbers, identifying distinct steady and periodic regimes. They also designed adaptive and sliding mode controllers that stabilized the system without prior knowledge of the Reynolds number, demonstrating effective control of both laminar and periodic states.

The control problem for the 2D Navier-Stokes equations remains an active area of research. While theoretical studies have provided significant insights, practical control strategies are still evolving. Early contributions by Guan et al. [23] proposed adaptive pinning control strategies for suppressing turbulence. Gambino et al. [24] designed adaptive controllers to stabilize fluid states toward steady solutions. More recently, Smaoui and Zribi [17–19] developed reduced-order models for forced Navier-Stokes systems with forcing applied to mode $(0, \alpha)$. For $\alpha = 4$, these models exhibit period-doubling bifurcations that eventually lead to chaotic attractors. They also introduced Lyapunov-based control strategies to steer the system toward desired fixed points or to synchronize multiple reduced-order models.

Complementary efforts have employed direct numerical simulations to understand turbulence onset and energy transfer. Musacchio and Boffetta [25] explored turbulent energy cascades in Kolmogorov flows. Suri et al. [26] developed improved quasi-two-dimensional models for electromagnetic forcing experiments. Mishra et al. [27] analyzed flow reversals and condensate formation in turbulent regimes. Tithof et al. [28] highlighted the importance of realistic boundary conditions when modeling bifurcation sequences.

Comprehensive reviews, such as the one by Fylladitakis [29], have synthesized the evolution of Kolmogorov flow research, emphasizing its role in studying turbulence, anisotropy, and hydrodynamic instabilities. Additionally, data-driven methods have emerged as powerful tools for analyzing high-dimensional fluid systems. Smaoui [4] explored dimensionality reduction techniques by applying both K-L decomposition and Autoassociative Neural Networks (ANNs) to dynamical systems governed by the one-dimensional Kuramoto-Sivashinsky equation and the two-dimensional Navier-Stokes equations. His study demonstrated that coherent structures and attractor dynamics could be effectively captured on low-dimensional nonlinear manifolds. Neural networks were shown to outperform traditional linear methods in terms of dimensionality reduction. More recently, De Jesús and Graham [5] used undercomplete autoencoders and neural networks to develop data-driven reduced-order models for chaotic and intermittent Kolmogorov flows. Their models successfully reproduced chaotic bursts, relative periodic orbits, and long-term flow statistics, showing the promise of machine learning in complex fluid modeling.

Altogether, these developments highlight major progress in understanding turbulence transitions using low-dimensional modeling, bifurcation analysis, control strategies, and modern data-driven methods. The combination of analytical, numerical, and machine learning techniques continues to deepen our understanding of complex fluid dynamics. These approaches offer promising directions for future research in turbulence control and prediction.

In this work, we construct a nine-mode reduced-order model derived from the two-dimensional Navier-Stokes equations, which significantly extends the bifurcation structure previously observed by Smaoui [15]. It is important to note that when restricted to a subset of modes, the new nine-mode system reduces exactly to the seven-mode system developed in [15], thereby maintaining consistency with prior formulations. We emphasize that the addition of two extra modes introduces new dynamical features, such as hysteresis and more intricate bifurcation patterns, that were not observed or captured in [15]. Furthermore, to regulate and control the complex behaviors exhibited by the system at different Reynolds numbers, we design and implement Lyapunov-based controllers. These controllers are shown to effectively stabilize both steady-state and periodic regimes, as well as mitigate chaotic oscillations.

The structure of the paper is as follows. Section 2 presents an analysis of the dynamics of the reduced-order model for the two-dimensional Kolmogorov flow across a range of Reynolds numbers. In Section 3, a Lyapunov-based control strategy is developed and implemented to stabilize the system at a fixed point, with validation through numerical simulations. Section 4 extends this approach by employing Lyapunov-based control and synchronization techniques to stabilize the system toward periodic orbits or chaotic attractors, also supported by numerical simulations. Finally, Section 5 presents the concluding remarks.

2. The 2D Navier-Stokes equations

2.1 *A nine-mode reduced order model of the 2D Navier-Stokes equations*

The so-called basic 2D Kolmogorov flow, given by $\overrightarrow{u} = (\alpha \sin(\alpha y),\ 0)$, was introduced by Kolmogorov [1] as a model for investigating the transition to turbulence. This flow represents an exact solution to the two-dimensional Navier-Stokes equations under periodic boundary conditions in both spatial directions, $0 \leq x,\ y \leq 2\pi$, and is governed by

$$\begin{aligned} &\overrightarrow{u_t} + (\overrightarrow{u} \cdot \nabla)\,\overrightarrow{u} + \nabla p = \nu \nabla^2 \overrightarrow{u} + \overrightarrow{f}, \\ &\nabla \cdot \overrightarrow{u} = 0, \end{aligned} \tag{1}$$

where $\boldsymbol{u} = (u_1,\ u_2)$ denotes the velocity field and the external force is given by $\boldsymbol{f} = (\alpha^3 \nu \sin(\alpha y),\ 0)$. The forcing is assumed to be steady and spatially biperiodic. The kinematic viscosity is defined as $\nu = \dfrac{1}{R_e}$, where R_e is the Reynolds number, and p denotes the pressure field.

In this paper, we follow the methodology outlined in [15]. Specifically, we derive a system of nine Ordinary Differential Equations (ODEs) from the Navier-Stokes equations by expanding the velocity field $\overrightarrow{u}$ in the following form:

$$\overrightarrow{u}(x) = \sum_{\mathbf{k} \neq 0} \exp(i\mathbf{k} \cdot \mathbf{x})\, \psi_{\mathbf{k}} \frac{\mathbf{k}^{\perp}}{|\mathbf{k}|}, \tag{2}$$

where $\mathbf{k}$= $(h_1,\ h_2)$ is a wave vector with integer components, $\mathbf{k}^{\perp} = (h_2,\ -h_1)$, and the reality condition $\psi_{\mathbf{k}} = -\overline{\psi}_{-\mathbf{k}}$ needs to be satisfied to ensure that the velocity field remains real.

The equation for $\{\psi_{\mathbf{k}}\}_{\mathbf{k} \neq 0}$ is

$$\dot{\psi}_{\mathbf{k}} = -i \sum_{\substack{\mathbf{k}_1 + \mathbf{k}_2 \\ + \mathbf{k} = 0}} \frac{(\mathbf{k}_1^{\perp} \cdot \mathbf{k}_2)(|\mathbf{k_2}|^2 - |\mathbf{k_1}|^2)}{2|\mathbf{k}_1||\mathbf{k}_2||\mathbf{k}|} \overline{\psi}_{\mathbf{k}_1} \overline{\psi}_{\mathbf{k}_2} - \nu |\mathbf{k}|^2 \psi_{\mathbf{k}} + f_{\mathbf{k}}, \tag{3}$$

where $\psi_{\mathbf{k}} = -\overline{\psi}_{-\mathbf{k}}$ and $f_{\mathbf{k}}$ is the component of $\overrightarrow{f}$ with respect to $\left(\dfrac{\mathbf{k}^{\perp}}{|\mathbf{k}|}\right) \exp(i\mathbf{k} \cdot \mathbf{x})$.

To construct a reduced-order model, we consider the following set of wave vectors: $\mathbf{k}_1 = (1,\ 1)$, $\mathbf{k}_2 = (0,\ 3)$, $\mathbf{k}_3 = (0,\ 2)$, $\mathbf{k}_4 = (1,\ 2)$, $\mathbf{k}_5 = (0,\ 1)$, $\mathbf{k}_6 = (1,\ 0)$, $\mathbf{k}_7 = (1,\ -2)$, $\mathbf{k}_8 = (1,\ 3)$, $\mathbf{k}_9 = (2,\ -1)$, along with their negatives in (3) to derive the following system of nine coupled Ordinary Differential Equations (ODEs) governing the dynamics of the selected modes:

$$\dot{\psi}_{\mathbf{k_1}} = -i\Big[\frac{-4}{\sqrt{10}}\psi_{\mathbf{k_2}}\psi_{\mathbf{k_7}} + \frac{3}{\sqrt{5}}\overline{\psi}_{\mathbf{k_3}}\psi_{\mathbf{k_8}} + \frac{4}{\sqrt{10}}\psi_{\mathbf{k_4}}\overline{\psi}_{\mathbf{k_5}}\Big] - 2\nu\psi_{\mathbf{k}_1} + f_{\mathbf{k_1}},$$

$$\dot{\psi}_{\mathbf{k_2}} = -i\Big[\frac{3}{\sqrt{10}}\psi_{\mathbf{k_1}}\overline{\psi}_{\mathbf{k_7}} + \frac{-9}{\sqrt{10}}\overline{\psi}_{\mathbf{k_6}}\psi_{\mathbf{k_8}}\Big] - 9\nu\psi_{\mathbf{k}_2} + f_{\mathbf{k_2}},$$

$$\dot{\psi}_{\mathbf{k_3}} = -i\Big[\frac{-4}{\sqrt{5}}\overline{\psi}_{\mathbf{k_1}}\psi_{\mathbf{k_8}} + \frac{4}{\sqrt{5}}\psi_{\mathbf{k_6}}\overline{\psi}_{\mathbf{k_7}} + \frac{-4}{\sqrt{5}}\psi_{\mathbf{k_4}}\overline{\psi}_{\mathbf{k_6}}\Big] - 4\nu\psi_{\mathbf{k}_3} + f_{\mathbf{k_3}},$$

$$\dot{\psi}_{\mathbf{k_4}} = -i\Big[\frac{1}{\sqrt{10}}\psi_{\mathbf{k_1}}\psi_{\mathbf{k_5}} + \frac{-3}{\sqrt{5}}\psi_{\mathbf{k_3}}\psi_{\mathbf{k_6}} + \frac{9}{5\sqrt{2}}\overline{\psi}_{\mathbf{k_5}}\psi_{\mathbf{k_8}}\Big] - 5\nu\psi_{\mathbf{k}_4} + f_{\mathbf{k_4}},$$

$$\dot{\psi}_{\mathbf{k_5}} = -i\Big[\frac{-3}{\sqrt{10}}\overline{\psi}_{\mathbf{k_1}}\psi_{\mathbf{k_4}} + \frac{-1}{\sqrt{2}}\psi_{\mathbf{k_1}}\overline{\psi}_{\mathbf{k_6}} + \frac{-1}{\sqrt{2}}\overline{\psi}_{\mathbf{k_4}}\psi_{\mathbf{k_8}}\Big] - \nu\psi_{\mathbf{k}_5} + f_{\mathbf{k_5}}, \tag{4}$$

$$\dot{\psi}_{\mathbf{k_6}} = -i\Big[\frac{1}{\sqrt{2}}\psi_{\mathbf{k_1}}\overline{\psi}_{\mathbf{k_5}} + \frac{1}{\sqrt{10}}\overline{\psi}_{\mathbf{k_2}}\psi_{\mathbf{k_8}} + \frac{1}{\sqrt{5}}\overline{\psi}_{\mathbf{k_3}}\psi_{\mathbf{k_4}} + \frac{1}{\sqrt{5}}\psi_{\mathbf{k_3}}\psi_{\mathbf{k_7}}\Big] - \nu\psi_{\mathbf{k}_6} + f_{\mathbf{k_6}},$$

$$\dot{\psi}_{\mathbf{k_7}} = -i\Big[\frac{-7}{\sqrt{10}}\psi_{\mathbf{k_1}}\overline{\psi}_{\mathbf{k_2}} + \frac{9}{5\sqrt{2}}\overline{\psi}_{\mathbf{k_1}}\psi_{\mathbf{k_9}} + \frac{-3}{\sqrt{5}}\overline{\psi}_{\mathbf{k_3}}\psi_{\mathbf{k_6}}\Big] - 5\nu\psi_{\mathbf{k}_7} + f_{\mathbf{k_7}},$$

$$\dot{\psi}_{\mathbf{k_8}} = -i\Big[\frac{-1}{\sqrt{5}}\psi_{\mathbf{k_1}}\psi_{\mathbf{k_3}} + \frac{-8}{\sqrt{10}}\psi_{\mathbf{k_2}}\psi_{\mathbf{k_6}} + \frac{4}{5\sqrt{2}}\psi_{\mathbf{k_4}}\psi_{\mathbf{k_5}}\Big] - 10\nu\psi_{\mathbf{k}_8} + f_{\mathbf{k_8}},$$

$$\dot{\psi}_{\mathbf{k_9}} = -i\Big[\frac{9}{5\sqrt{2}}\psi_{\mathbf{k_1}}\psi_{\mathbf{k_7}}\Big] - 5\nu\psi_{\mathbf{k}_9} + f_{\mathbf{k_9}}.$$

Let $\psi_{\mathbf{k}_1} = ix_1$, $\psi_{\mathbf{k}_2} = x_2$, $\psi_{\mathbf{k}_3} = -ix_3$, $\psi_{\mathbf{k}_4} = x_4$, $\psi_{\mathbf{k}_5} = x_5$, $\psi_{\mathbf{k}_6} = x_6$, $\psi_{\mathbf{k}_7} = x_7$, $\psi_{\mathbf{k}_8} = -ix_8$, and $\psi_{\mathbf{k}_9} = x_9$, then system (4) becomes:

$$\dot{x}_1 = \frac{4}{\sqrt{10}}x_2x_7 - \frac{3}{\sqrt{5}}x_3x_8 - \frac{4}{\sqrt{10}}x_4x_5 - 2\nu x_1 - if_{\mathbf{k_1}},$$

$$\dot{x}_2 = \frac{3}{\sqrt{10}}x_1x_7 + \frac{9}{\sqrt{10}}x_6x_8 - 9\nu x_2 + f_{\mathbf{k_2}},$$

$$\dot{x}_3 = \frac{4}{\sqrt{5}}x_1x_8 + \frac{4}{\sqrt{5}}x_6x_7 - \frac{4}{\sqrt{5}}x_4x_6 - 4\nu x_3 + if_{\mathbf{k_3}},$$

$$\dot{x}_4 = \frac{1}{\sqrt{10}}x_1x_5 + \frac{3}{\sqrt{5}}x_3x_6 - \frac{9}{5\sqrt{2}}x_5x_8 - 5\nu x_4 + f_{\mathbf{k_4}},$$

$$
\begin{aligned}
\dot{x}_5 &= \frac{3}{\sqrt{10}}x_1x_4 - \frac{1}{\sqrt{2}}x_1x_6 + \frac{1}{\sqrt{2}}x_4x_8 - \nu x_5 + f_{\mathbf{k_5}},\\
\dot{x}_6 &= \frac{1}{\sqrt{5}}x_1x_5 - \frac{1}{\sqrt{10}}x_2x_8 + \frac{1}{\sqrt{5}}x_3x_4 - \frac{1}{\sqrt{5}}x_3x_7 - \nu x_6 + f_{\mathbf{k_6}},\\
\dot{x}_7 &= \frac{-7}{\sqrt{10}}x_1x_2 - \frac{9}{5\sqrt{2}}x_1x_9 - \frac{3}{\sqrt{5}}x_3x_6 - 5\nu x_7 + f_{\mathbf{k_7}},\\
\dot{x}_8 &= \frac{-1}{\sqrt{5}}x_1x_3 - \frac{8}{5\sqrt{10}}x_2x_6 + \frac{4}{5\sqrt{2}}x_4x_5 - 10\nu x_8 + if_{\mathbf{k_8}},\\
\dot{x}_9 &= \frac{9}{5\sqrt{2}}x_1x_7 - 5\nu x_9 + f_{\mathbf{k_9}}.
\end{aligned}
\tag{5}
$$

By rescaling the length as $x_i = \sqrt{10}\nu\tilde{x}_i$ for $i = 1, \ldots, 9$, redefining the time variable as $t = \dfrac{\tilde{t}}{\nu}$ with $\nu = \dfrac{1}{2\sqrt{10}}\tilde{\nu}$, and assuming the forcing term acts on mode k_3, system (5) transforms into:

$$
\begin{aligned}
\dot{x}_1 &= -2x_1 + 4x_2x_7 - 3\sqrt{2}x_3x_8 - 4x_4x_5,\\
\dot{x}_2 &= -9x_2 + 3x_1x_7 + 9x_6x_8,\\
\dot{x}_3 &= -4x_3 + 4\sqrt{2}x_1x_8 + 4\sqrt{2}x_6x_7 - 4\sqrt{2}x_4x_6 + 8R_e,\\
\dot{x}_4 &= -5x_4 + x_1x_5 + 3\sqrt{2}x_3x_6 - \frac{9\sqrt{5}}{5}x_5x_8,\\
\dot{x}_5 &= -x_5 + 3x_1x_4 - \sqrt{5}x_1x_6 + \sqrt{5}x_4x_8,\\
\dot{x}_6 &= -x_6 + \sqrt{5}x_1x_5 - x_2x_8 + \sqrt{2}x_3x_4 - \sqrt{2}x_3x_7,\\
\dot{x}_7 &= -5x_7 - 7x_1x_2 - \frac{9\sqrt{5}}{5}x_1x_9 - 3\sqrt{2}x_3x_6,\\
\dot{x}_8 &= -10x_8 - \sqrt{2}x_1x_3 - 8x_2x_6 + \frac{4\sqrt{5}}{5}x_4x_5,\\
\dot{x}_9 &= -5x_9 + \frac{9\sqrt{5}}{5}x_1x_7.
\end{aligned}
\tag{6}
$$

The system given by the equations in (6) can be written in the compact form:

$$\dot{x} = Ax + f(x), \tag{7}$$

where the vector $x = \begin{bmatrix} x_1 & x_2 & x_3 & x_4 & x_5 & x_6 & x_7 & x_8 & x_9 \end{bmatrix}^T$ and the diagonal matrix A is such that:

$$A = \text{diag}(-2,\ -9,\ -4,\ -5,\ -1,\ -1,\ -5,\ -10,\ -5), \tag{8}$$

and the nonlinear vector $f(x)$ is such that

$$f(x) = \begin{bmatrix} f_1 & f_2 & f_3 & f_4 & f_5 & f_6 & f_7 & f_8 & f_9 \end{bmatrix}^T, \tag{9}$$

with

$$\begin{aligned}
f_1 &= 4x_2x_7 - 3\sqrt{2}x_3x_8 - 4x_4x_5,\\
f_2 &= 3x_1x_7 + 9x_6x_8,\\
f_3 &= 4\sqrt{2}x_1x_8 + 4\sqrt{2}x_6x_7 - 4\sqrt{2}x_4x_6 + 8R_e,\\
f_4 &= x_1x_5 + 3\sqrt{2}x_3x_6 - \frac{9\sqrt{5}}{5}x_5x_8,\\
f_5 &= 3x_1x_4 - \sqrt{5}x_1x_6 + \sqrt{5}x_4x_8,\\
f_6 &= \sqrt{5}x_1x_5 - x_2x_8 + \sqrt{2}x_3x_4 - \sqrt{2}x_3x_7,\\
f_7 &= -7x_1x_2 - \frac{9\sqrt{5}}{5}x_1x_9 - 3\sqrt{2}x_3x_6,\\
f_8 &= -\sqrt{2}x_1x_3 - 8x_2x_6 + \frac{4\sqrt{5}}{5}x_4x_5,\\
f_9 &= \frac{9\sqrt{5}}{5}x_1x_7.
\end{aligned} \tag{10}$$

Remark It can be checked that system (6) remains invariant under the following three symmetries:

$$
\begin{aligned}
r_x &: (x_1, x_2, x_3, x_4, x_5, x_6, x_7, x_8, x_9) \Longleftrightarrow (x_1, -x_2, x_3, -x_4, -x_5, -x_6, -x_7, x_8, -x_9),\\
r_y &: (x_1, x_2, x_3, x_4, x_5, x_6, x_7, x_8, x_9) \Longleftrightarrow (-x_1, -x_2, x_3, x_4, -x_5, x_6, x_7, -x_8, -x_9),\\
r_o &: (x_1, x_2, x_3, x_4, x_5, x_6, x_7, x_8, x_9) \Longleftrightarrow (-x_1, x_2, x_3, -x_4, x_5, -x_6, -x_7, -x_8, x_9).
\end{aligned} \tag{11}
$$

where r_x, r_y and r_o represent reflection symmetries across the x-axis, the y-axis, and the origin, respectively.

2.2 *The dynamics of the nine-mode reduced-order model*

In this section, we analyze the dynamics of the reduced nine-dimensional system (6) for different Reynolds numbers R_e, as time evolves from $t = 0$ to $t = 100$ with a time step $\Delta t = 0.001$.

(i) For $0 \leq R_e \leq R_1 \simeq 0.3227$, the system exhibits a single fixed point: the basic state $P_0 = (0, 0, 2R_e, 0, 0, 0, 0, 0, 0)$, which remains globally asymptotically stable (see Figure 1a).

(ii) For $R_1 < R_e \leq R_2 \simeq 0.9128$, three fixed points are present: the original fixed point P_0, which becomes unstable due to a real eigenvalue crossing the imaginary axis, and two new stable fixed points, P_1 and P_2, that bifurcate from P_0 (see Figure 1b).

(iii) For $R_2 < R_e \leq R_3 \simeq 1.2698$, the system admits five fixed points: two asymptotically stable and three unstable (see Figure 1c).

(iv) or $R_3 < R_e \leq R_4 \simeq 15.941$, nine fixed points appear: four are asymptotically stable and five are unstable (see Figure 1d). Figure 2 illustrates the phase portrait of the four stable fixed points at $R_e = 10$. In Figure 2, the first asymptotically stable fixed point (top left) is obtained using the following initial conditions: $(x_1, x_2, x_3, x_4, x_5, x_6, x_7, x_8, x_9) = (-0.8275, -0.4703, 0.7234, -2.3355, -0.122, -3.599, 0.4255, -0.4234, -0.9355)$; the second asymptotically stable fixed point (bottom right) is obtained using the initial conditions: $(x_1, x_2, x_3, x_4, x_5, x_6, x_7, x_8, x_9) = (0.8275, -0.4703, 0.7234, 2.3355, -0.1220, 3.5990, -0.4255, 0.4234, -0.9355) = r_o(-0.8275, -0.4703, 0.7234, -2.3355, -0.122, -3.599, 0.4255, -0.4234, -0.9355)$; the third asymptotically stable fixed point (bottom left) is generated using the initial conditions: $(x_1, x_2, x_3, x_4, x_5, x_6, x_7, x_8, x_9) = (-0.8275, 0.4703, 0.7234, 2.3355, 0.1220, 3.5990, -0.4255, -0.4234, 0.9355) = r_x(-0.8275, -0.4703, 0.7234, -2.3355, -0.122, -3.599, 0.4255, -0.4234, -0.9355)$; the fourth asymptotically stable fixed point (top right) is generated using the initial conditions: $(x_1, x_2, x_3, x_4, x_5, x_6, x_7, x_8, x_9) = (0.8275, 0.4703, 0.7234, -2.3355, 0.1220, -3.5990, 0.4255, 0.4234, 0.9355) = r_y(-0.8275, -0.4703, 0.7234, -2.3355, -0.122, -3.599, 0.4255, -0.4234, -0.9355)$.

(v) For $R_4 < R_e \leq R_5 \simeq 20.378$, a Hopf bifurcation occurs. The four stable fixed points lose stability as a pair of complex conjugate eigenvalues cross the imaginary axis, leading to the emergence of four stable periodic orbits. The five previously unstable fixed points remain unstable (see Figure 1e). Figure 3 depicts the phase portrait of the stable periodic orbits at $R_e = 17$.

(vi) For $R_5 < R_e \leq R_6 \simeq 20.4543$, each periodic orbit undergoes a period-doubling bifurcation, producing new stable periodic orbits with twice the original period. Figure 4 shows the corresponding phase portrait at $R_e = 20.4$.

(vii) For $R_6 < R_e \leq R_7 \simeq 20.508$, a homoclinic gluing bifurcation takes place, resulting in two large periodic orbits connecting pairs of the previously stable periodic orbits. Figure 5 presents two switching states and their time series near the bifurcation point $R_e = 20.4544$, while Figure 6 illustrates the two stable periodic orbits at $R_e = 20.5$. Notably, the switching behavior observed at $R_e = 20.4544$ vanishes, giving rise to stable periodic motion.

(viii) For $R_7 < R_e \leq R_8 \simeq 20.5112$, the two large periodic orbits bifurcate into four new stable periodic orbits. Each new orbit connects a pair of the periodic orbits observed in (vi). Figure 7 displays the phase portrait and time series of these four orbits at $R_e = 20.5112$, confirming their periodic nature. In Figure 7, the first stable periodic orbit (first left) and its time series (first right) are obtained using the following initial conditions: $x_1(0) = (-0.8275, -0.4703, 0.7234, -2.3355, -0.122, -3.599, 0.4255, -0.4234, -0.9355)$; the second periodic orbit (second

left) and time series (second right) are obtained using $x_2(0) = (0.8275, 0.4703, 0.7234, -2.3355, 0.1220, -3.5990, 0.4255, 0.4234, 0.9355) = r_y x_1(0)$; the third stable periodic orbit (third left) and time series (third right) are generated using $x_3(0) = (-0.8275, 0.4703, 0.7234, 2.3355, 0.1220, 3.5990, -0.4255, -0.4234, 0.9355) = r_x x_1(0)$; the fourth one (fourth left) and time series (fourth right) are generated using $x_4(0) = (0.8275, -0.4703, 0.7234, 2.3355, -0.1220, 3.5990, -0.4255, 0.4234, -0.9355) = r_o x_1(0)$. The time series shows that behavior is periodic.

(ix) For $R_8 < R_e \leq R_9 \simeq 20.8288$, the four periodic orbits lose stability, giving rise to four chaotic or strange attractors. Figure 8 shows the phase portraits and time series of these chaotic attractors at $R_e = 20.7$. In Figure 8, the first chaotic attractor (first left) and its time series (first right) are obtained using the following initial conditions: $x_1(0) = (-0.8275, -0.4703, 0.7234, -2.3355, -0.122, -3.599, 0.4255, -0.4234, -0.9355)$; the second chaotic attractor (second left) and time series (second right) are obtained using $x_2(0) = (0.7275, 0.5, 0.6, -2.3355, 0, -2.5990, 0.2255, 0.3234, 0.8355)$; the third chaotic attractor orbit (third left) and time series (third right) are generated using $x_3(0) = (-0.8275, 0.4703, 0.7234, 2.3355, 0.1220, 3.5990, -0.4255, -0.4234, 0.9355)$; the fourth one (fourth left) and time series (fourth right) are generated using $x_4(0) = (0.7275, -0.5, 0.6, 2.3355, 0, 325990, -0.2255, 0.3234, -0.8355)$. The time series shows that behavior is chaotic.

(x) For $R_9 < R_e \leq 30$, the chaotic attractors undergo further bifurcations, leading to the emergence of two new stable periodic orbits (see Figure 9). Extensive numerical simulations reveal that these periodic orbits remain stable not only for $R_9 < R_e \leq 30$, but also within the range $19.9136 \leq R_e \leq R_9 \simeq 20.8288$. Figure 10 displays two stable periodic orbits at $R_e = 19.2$ and $R_e = 20.3$, respectively, which coexist with previously identified attractors in stages (v) through (ix), particularly within the range $19.9136 \leq R_e \leq R_9 \simeq 20.8288$, illustrating pronounced multi-stability and hysteresis in the system's long-term dynamics.

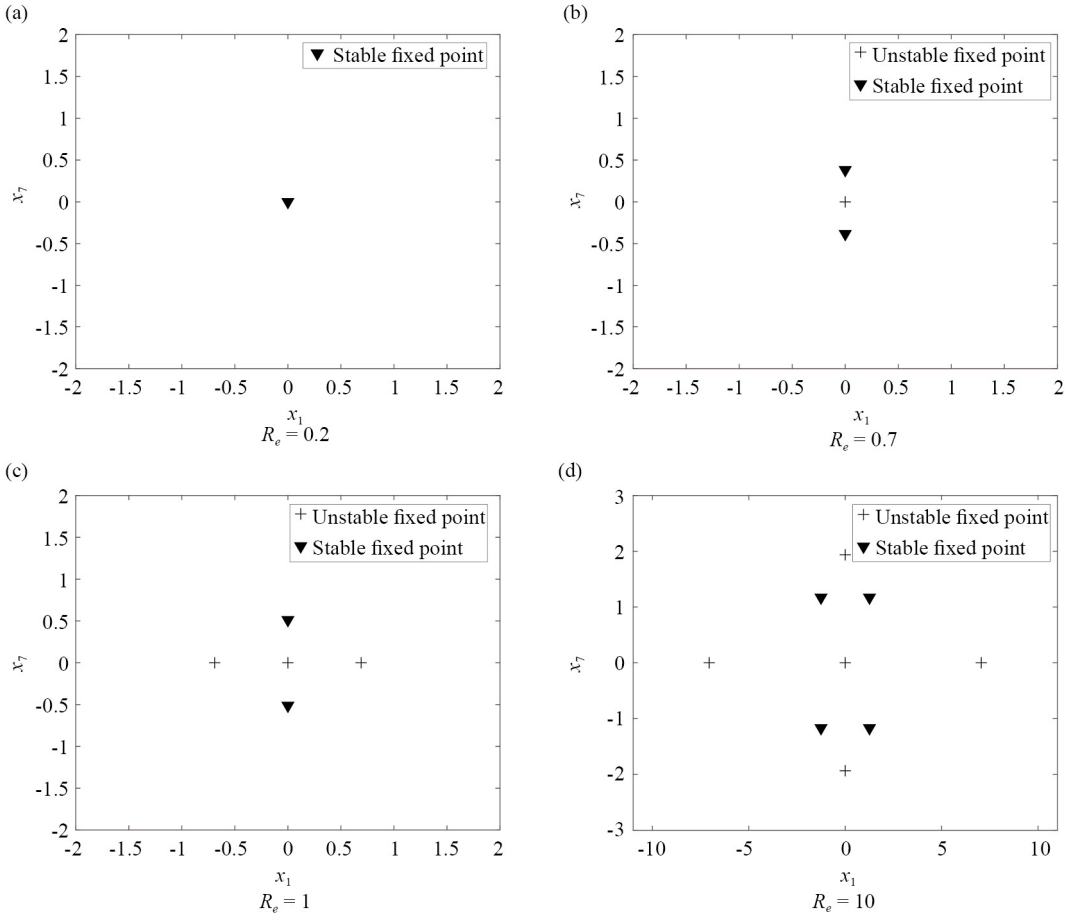

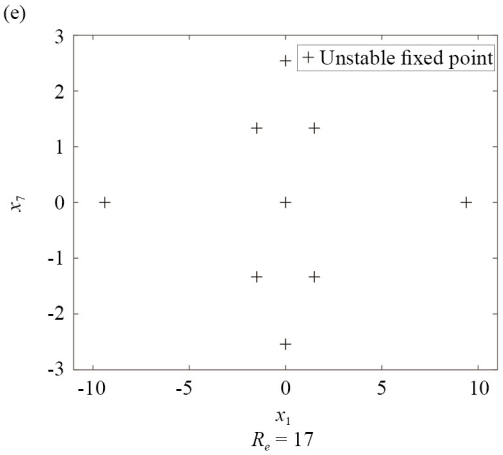

Figure 1. Bifurcation sequence of equilibrium points as the Reynolds number R_e increases. The system transitions from a single stable fixed point to multiple coexisting stable and unstable equilibria through successive bifurcations

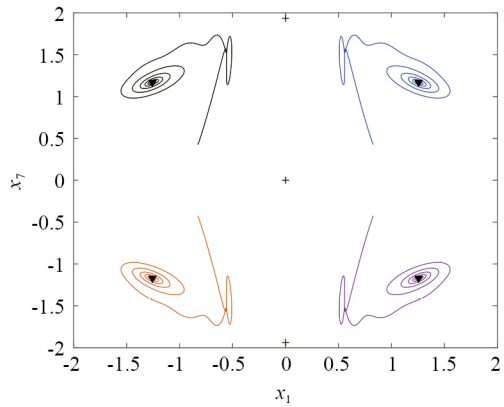

Figure 2. Phase portraits of the four asymptotically stable fixed points at $R_e = 10$, generated from symmetric initial conditions related by the reflection symmetries r_x, r_y, and r_o

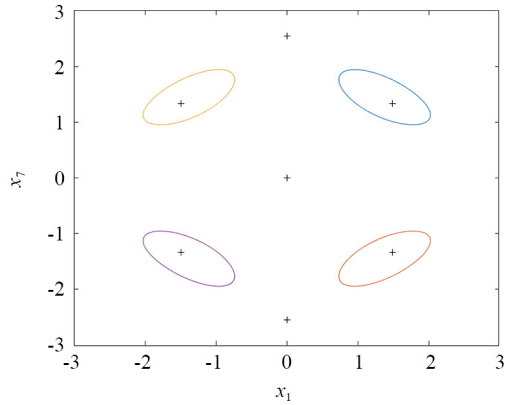

Figure 3. Phase portraits of the four stable periodic orbits that emerge after a Hopf bifurcation at $R_e = 17$, resulting from the loss of stability of the corresponding fixed points

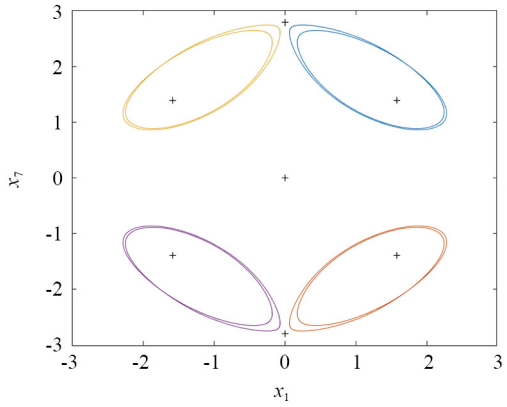

Figure 4. Phase portraits of the four stable periodic orbits at $R_e = 20.4$ following a period-doubling bifurcation. Each orbit exhibits twice the period of the original cycles observed before the bifurcation

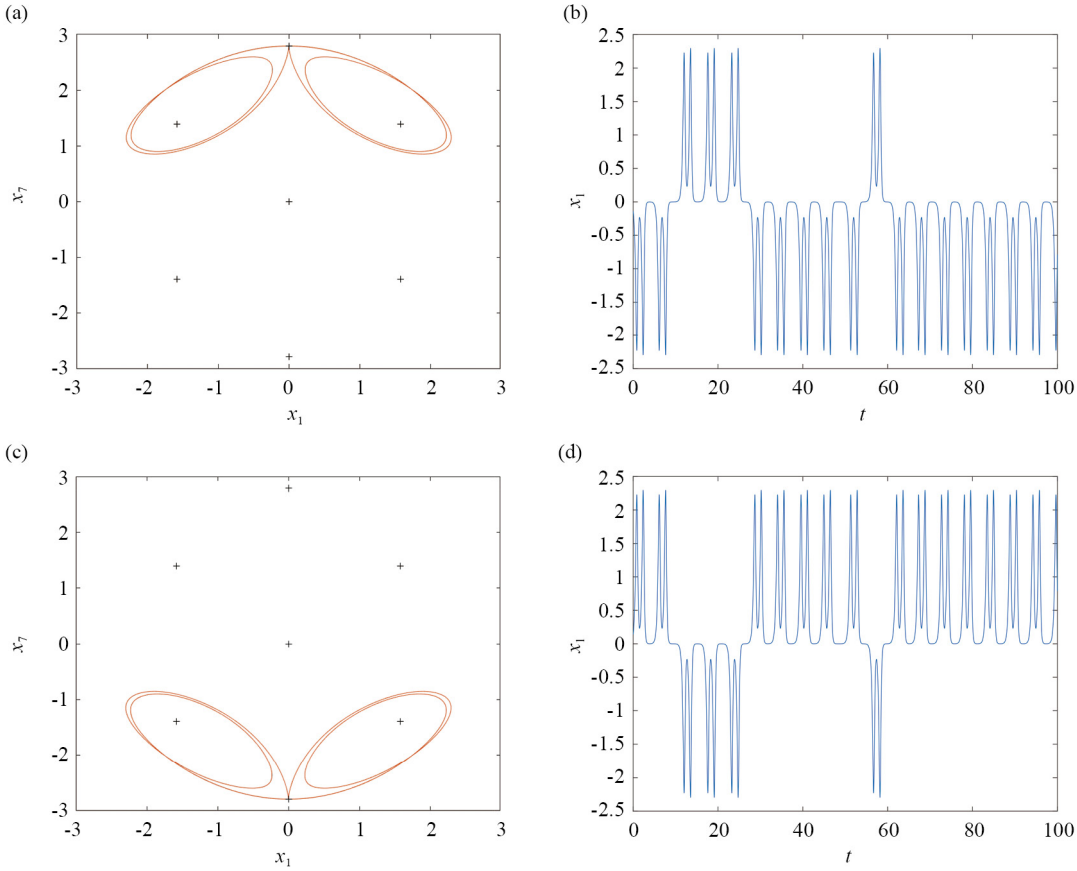

Figure 5. Switching dynamics near the homoclinic gluing bifurcation at $R_e = 20.4544$. The figure shows two transient switching states and their associated time series, illustrating the system's sensitivity near the bifurcation threshold

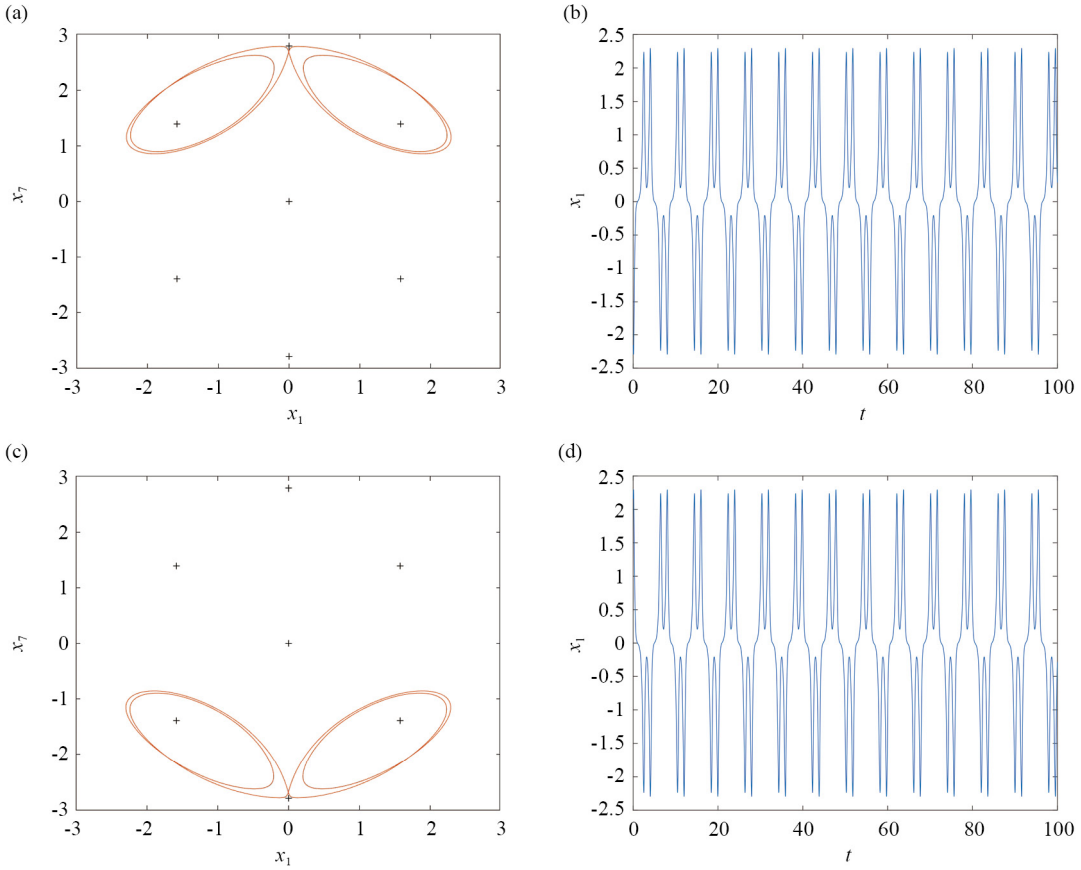

Figure 6. Two stable periodic orbits at $R_e = 20.5$, obtained after the homoclinic gluing bifurcation. The switching behavior previously observed at $R_e = 20.4544$ (see Figure 5) is no longer present, giving rise to stable and regular periodic motion

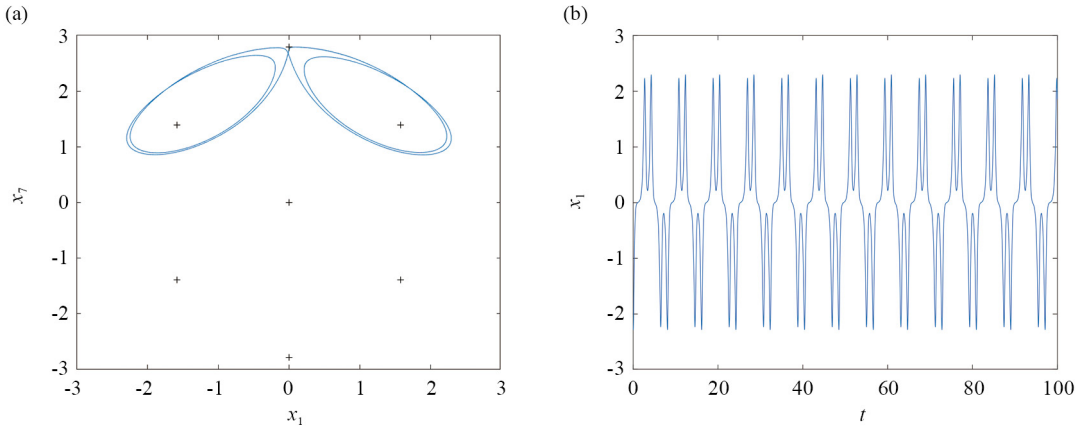

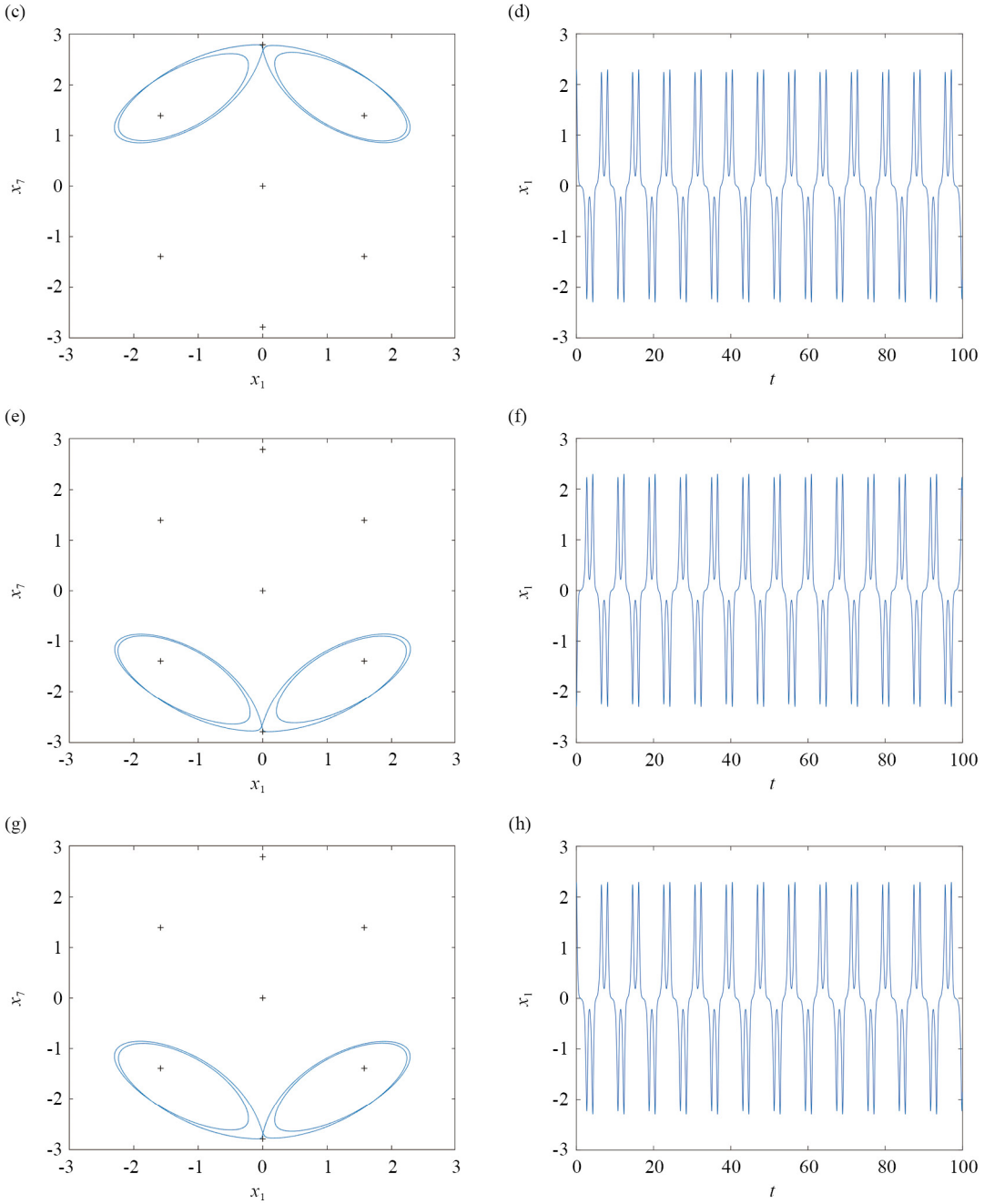

Figure 7. Four stable periodic orbits at $R_e = 20.5112$ emerging from a bifurcation of the two large periodic orbits shown in Figure 6. Each new orbit connects pairs of earlier periodic orbits and corresponds to a symmetric initial condition generated via the transformations r_x, r_y, and r_o. The phase portraits and time series confirm the periodic nature of all four orbits

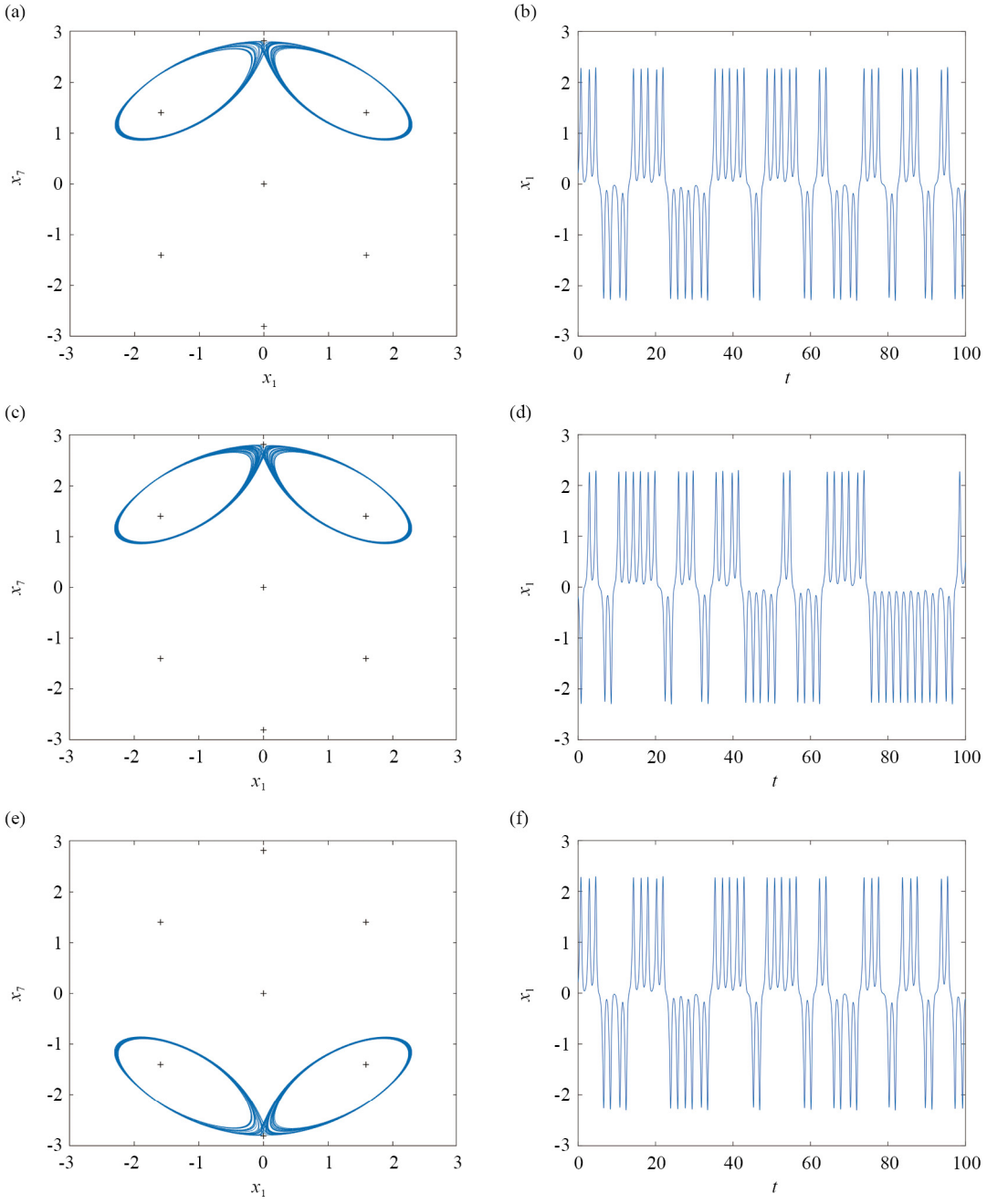
(a)
(b)
(c)
(d)
(e)
(f)
x_7
x_1
t

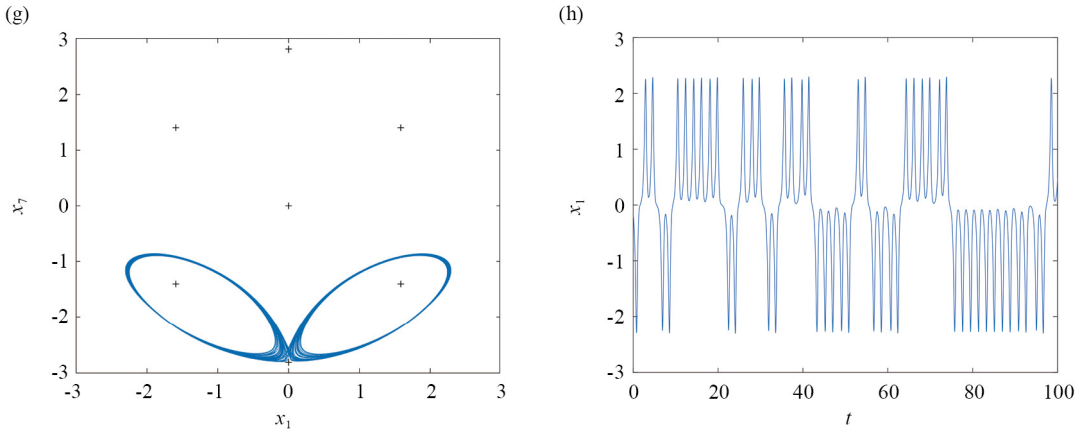

Figure 8. Four chaotic attractors at $R_e = 20.7$ that arise following the loss of stability of the periodic orbits shown in Figure 7. The phase portraits and corresponding time series demonstrate the onset of chaos. These attractors result from symmetry-related initial conditions and confirm the emergence of complex dynamics beyond the period-doubling and gluing bifurcations

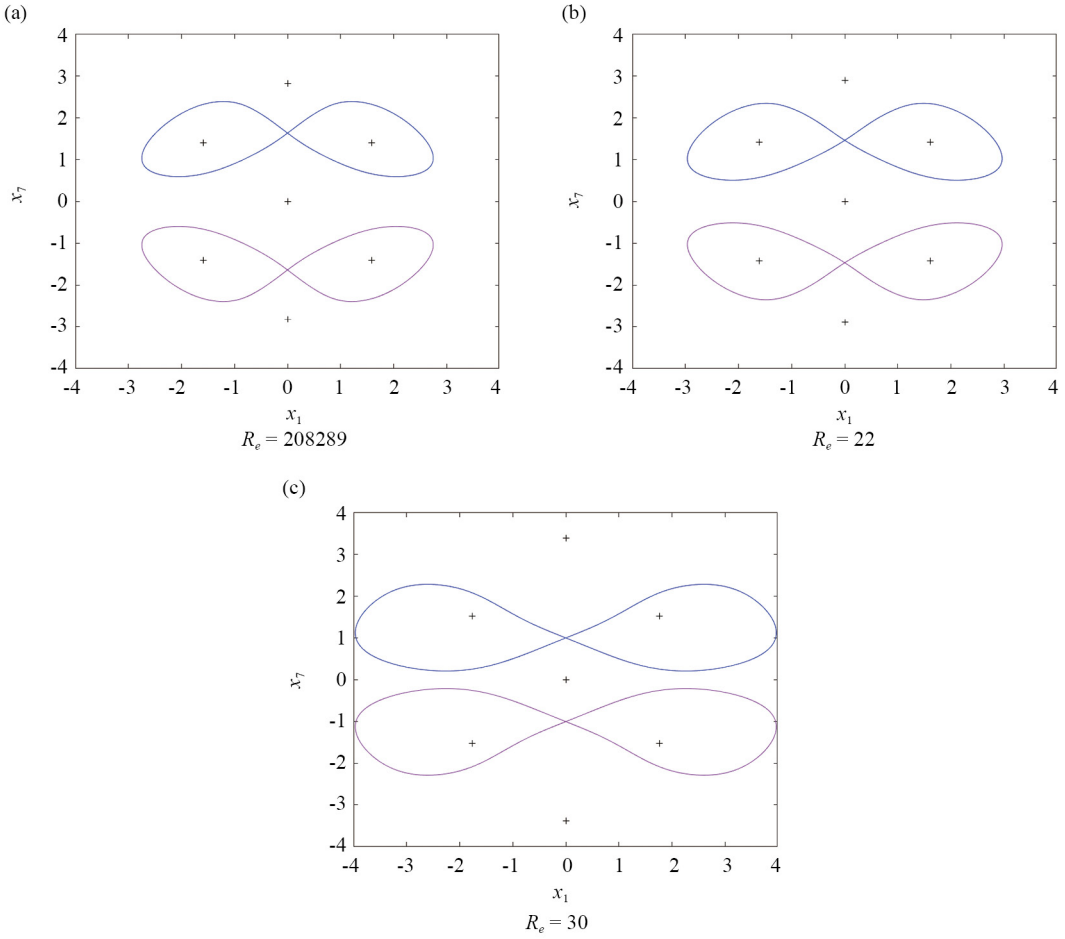

Figure 9. Two new stable periodic orbits at $R_e = 25$ that emerge following further bifurcations of the chaotic attractors observed in earlier regimes

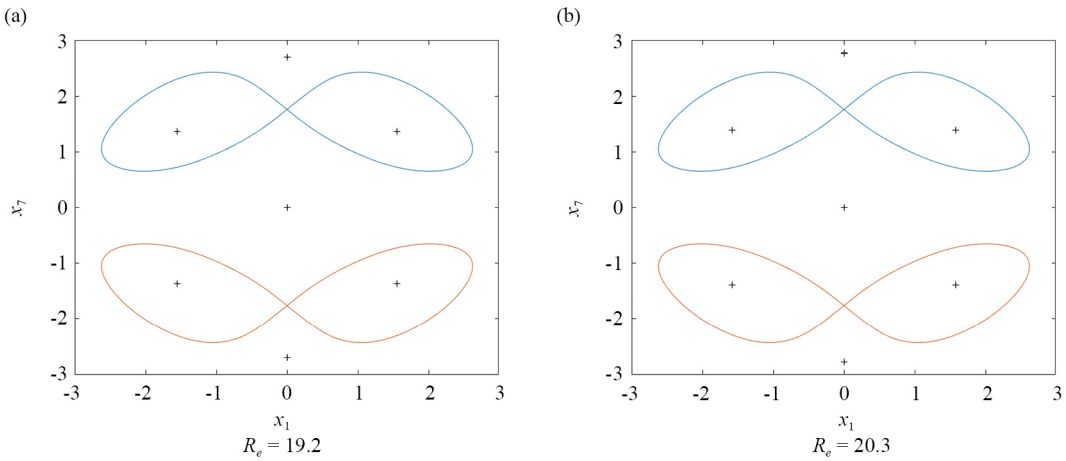

Figure 10. Two stable periodic orbits at $R_e = 19.2$ and $R_e = 20.3$, respectively, coexist with previously identified attractors in the range $19.9136 \leq R_e \leq R_9 \simeq 20.8288$, illustrating pronounced multi-stability and hysteresis in the system's long-term dynamics

3. Control of the dynamics of the reduced-order model to a fixed point

In this section, a Lyapunov-based control strategy is developed to drive the system states toward a specified fixed point, regardless of its stability (See Appendix A.1 for the controller design).

The simulation results for system (24), using the control scheme defined in (30), are presented below. Simulations are conducted for two cases corresponding to Reynolds numbers $R_e = 19$ and $R_e = 21$, with initial conditions $X_1(0)$ and $X_2(0)$, respectively.

The initial condition for $R_e = 19$ is given by

$$X_1(0) = \begin{bmatrix} -1.5464 & -0.1020 & 0.8329 & -3.6684 & -0.2004 & -5.2523 & 1.3692 & -0.1150 & -1.7045 \end{bmatrix}^T. \quad (12)$$

Here, $X_1(0)$ corresponds to one of the unstable fixed points of the system (6) at $R_e = 19$. The associated desired fixed points are:

$$\begin{aligned} X_{1d} &= \begin{bmatrix} -1.5464 & -0.1020 & 0.8329 & -3.6684 & -0.2004 & -5.2523 & 1.3692 & -0.1150 & -1.7045 \end{bmatrix}^T, \\ X_{2d} &= \begin{bmatrix} -1.5464 & 0.1020 & 0.8329 & 3.6684 & 0.2004 & 5.2523 & -1.3692 & -0.1150 & 1.7045 \end{bmatrix}^T, \\ X_{3d} &= \begin{bmatrix} 1.5464 & 0.1020 & 0.8329 & -3.6684 & 0.2004 & -5.2523 & 1.3692 & 0.1150 & 1.7045 \end{bmatrix}^T, \\ X_{4d} &= \begin{bmatrix} 1.5464 & -0.1020 & 0.8329 & 3.6684 & -0.2004 & 5.2523 & -1.3692 & 0.1150 & -1.7045 \end{bmatrix}^T. \end{aligned} \quad (13)$$

Similarly, the initial condition for $R_e = 21$ is:

$$X_2(0) = \begin{bmatrix} -1.5928 & -0.0992 & 0.8342 & -3.8814 & -0.1959 & -5.5456 & 1.4010 & -0.1162 & -1.7963 \end{bmatrix}^T. \quad (14)$$

The point $X_2(0)$ represents an unstable fixed point of the system (6) at $R_e = 21$. The corresponding desired fixed points are:

$$\begin{aligned} X_{1d} &= \begin{bmatrix} -1.5928 & -0.0992 & 0.8342 & -3.8814 & -0.1959 & -5.5456 & 1.4010 & -0.1162 & -1.7963 \end{bmatrix}^T, \\ X_{2d} &= \begin{bmatrix} -1.5928 & 0.0992 & 0.8342 & 3.8814 & 0.1959 & 5.5456 & -1.4010 & -0.1162 & 1.7963 \end{bmatrix}^T, \\ X_{3d} &= \begin{bmatrix} 1.5928 & 0.0992 & 0.8342 & -3.8814 & 0.1959 & -5.5456 & 1.4010 & 0.1162 & 1.7963 \end{bmatrix}^T, \\ X_{4d} &= \begin{bmatrix} 1.5928 & -0.0992 & 0.8342 & 3.8814 & -0.1959 & 5.5456 & -1.4010 & 0.1162 & -1.7963 \end{bmatrix}^T. \end{aligned} \quad (15)$$

It must be noted that the desired fixed points listed in (13) and (15) were originally asymptotically stable but became unstable due to the occurrence of a Hopf bifurcation.

The control gains used in the simulations are as follows: $c_i = 10$ for $i = 1, \ldots, 4$, and

$$a_1 = 1, \quad a_2 = 7, \quad a_3 = 1, \quad a_4 = 3.5, \quad a_5 = 1, \quad a_6 = 1, \quad a_7 = 3, \quad a_8 = 7.875, \quad a_9 = 3. \quad (16)$$

The control inputs u_i, for $i = 1, \ldots, 4$, are set to zero during the first $100,000\ \Delta t$ time steps. After this time, the control law given by (30) is periodically switched on and off. When the control is activated, the target state x_d is set to one of the four desired fixed points.

At $R_e = 19$, the dynamics of the system (6) exhibit four stable periodic orbits, while at $R_e = 21$, the dynamics reduce to two stable periodic orbits.

The simulation results for $R_e = 19$ are shown in Figures 11 and 12. Figure 11 presents the phase portrait of the controlled states $x_7(t)$ versus $x_1(t)$ as the control is switched on and off for $t \in [0,\ 800]$. Specifically:

• Figure 11a shows the uncontrolled dynamics for $t \in [0,\ 100]$, resulting in the first stable periodic orbit.

• Figure 11b illustrates the controlled dynamics for $t \in [100.001,\ 200]$, where the states $x_i(t)$, $i = 1, \ldots, 9$, converge to X_{2d}.

• In Figure 11c, the control is switched off for $t \in [200.001,\ 300]$, producing the second stable periodic orbit.

• Figure 11d displays the system behavior under control for $t \in [300.001,\ 400]$, leading to convergence toward X_{3d}.

• Figure 11e captures the uncontrolled dynamics for $t \in [400.001,\ 500]$, generating the third stable periodic orbit.

• Figure 11f shows the controlled dynamics for $t \in [500.001,\ 600]$, with the states converging to X_{4d}.

• In Figure 11g, the control is again switched off for $t \in [600.001,\ 700]$, resulting in the fourth stable periodic orbit.

• Finally, Figure 11h illustrates the controlled behavior for $t \in [700.001,\ 800]$, where the states converge back to X_{1d}.

Figure 12 shows the time evolution of the controlled states $x_i(t)$, for $i = 1, \ldots, 9$, clearly depicting the switching between periodic behaviors when the control is off and convergence to the desired fixed points when the control is active.

These figures depict how the system's states $x_i(t)$ systematically converge to the designated fixed points during control activation and return to periodic orbits when the control is deactivated.

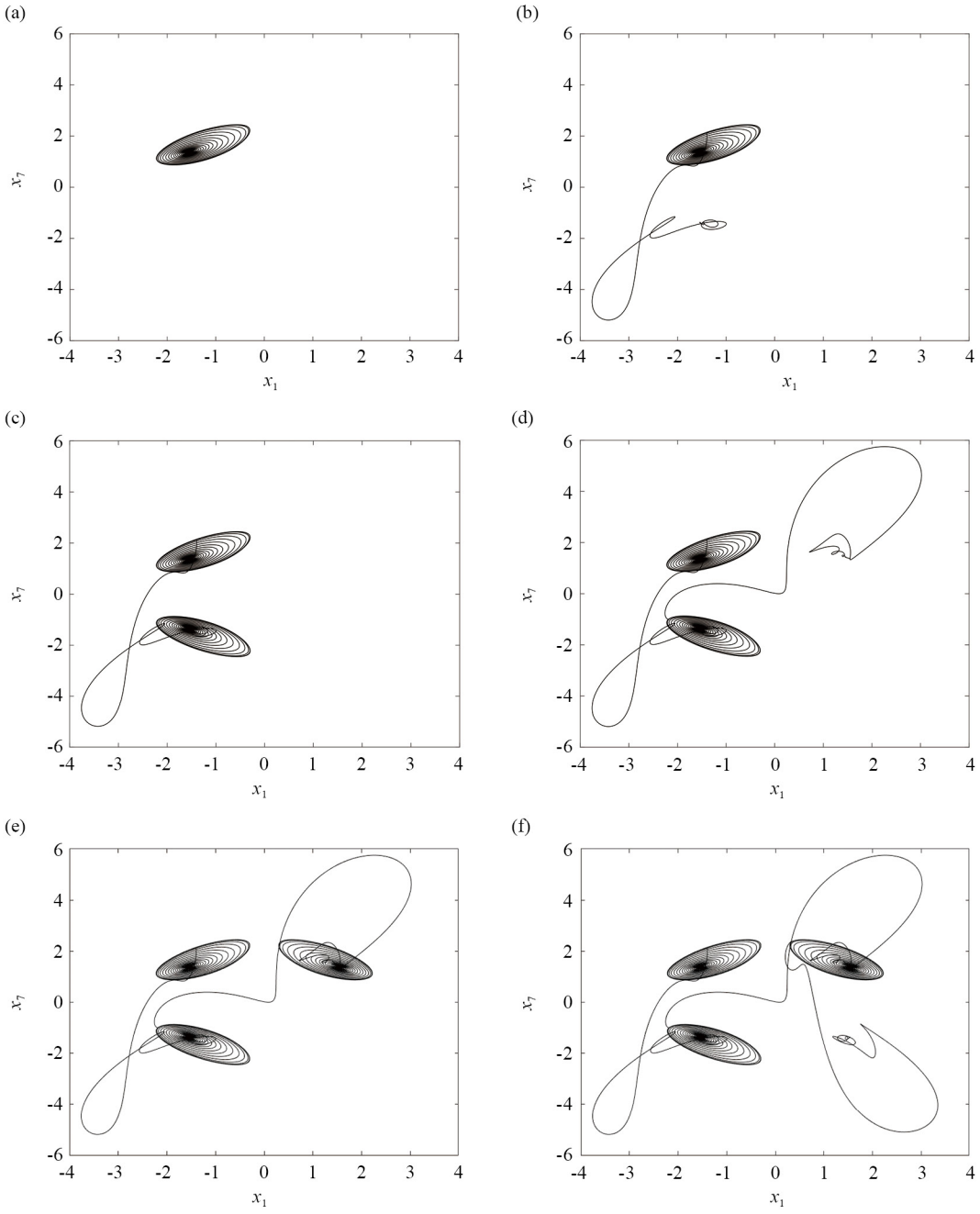
(a)
(b)
(c)
(d)
(e)
(f)
x_1
x_7

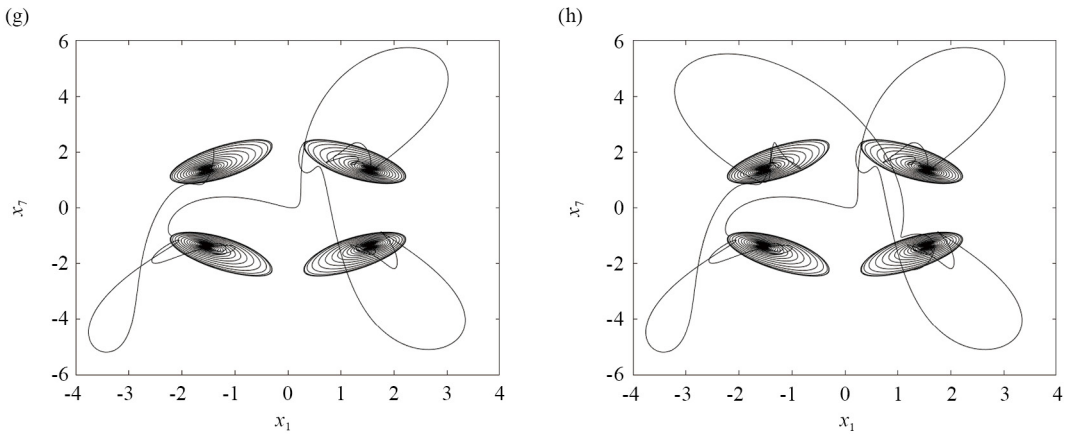

Figure 11. Phase portraits of the controlled and uncontrolled dynamics at $R_e = 19$, showing $x_7(t)$ versus $x_1(t)$ over the time interval $t \in [0,\ 800]$. Subfigures (a), (c), (e), and (g) show the system's natural evolution without control, resulting in transitions between four stable periodic orbits. Subfigures (b), (d), (f), and (h) illustrate the controlled dynamics during which the system is steered toward target states X_{2d}, X_{3d}, X_{4d}, and finally back to X_{1d}. This sequence highlights the controller's effectiveness in cycling through multiple coexisting attractors

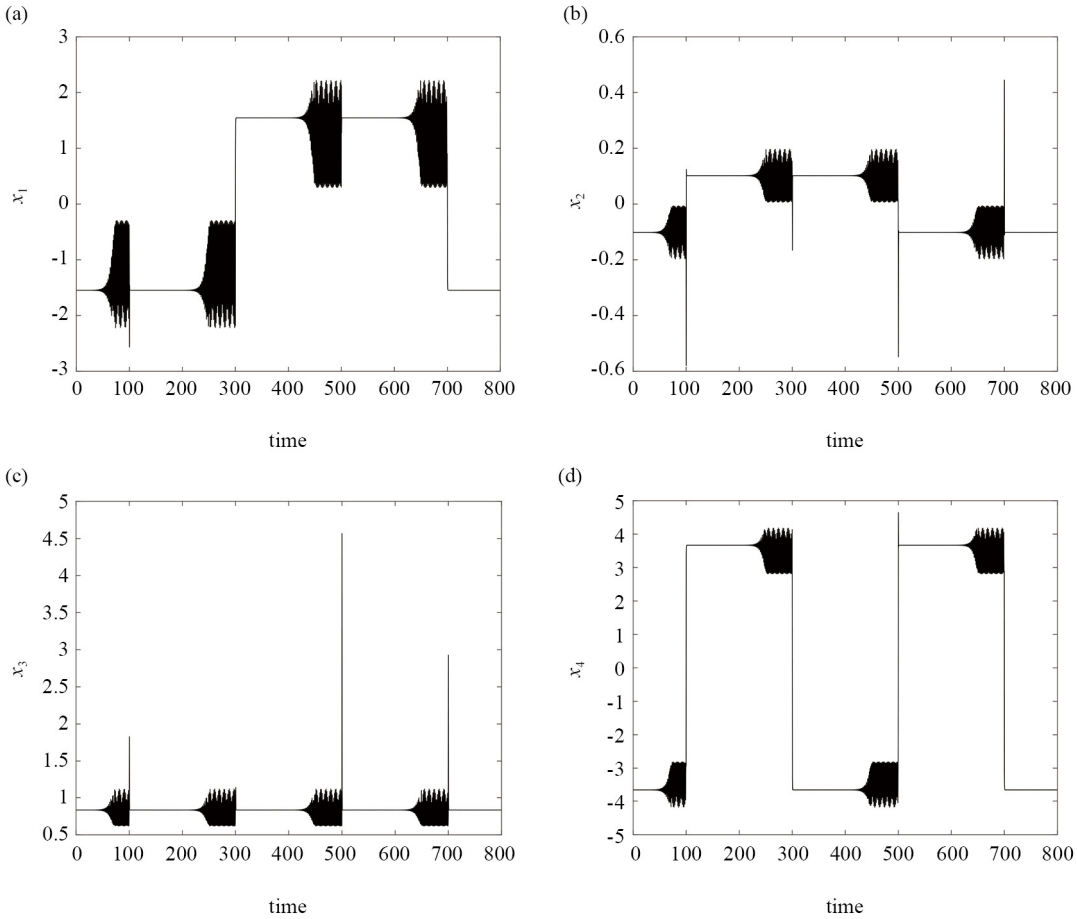

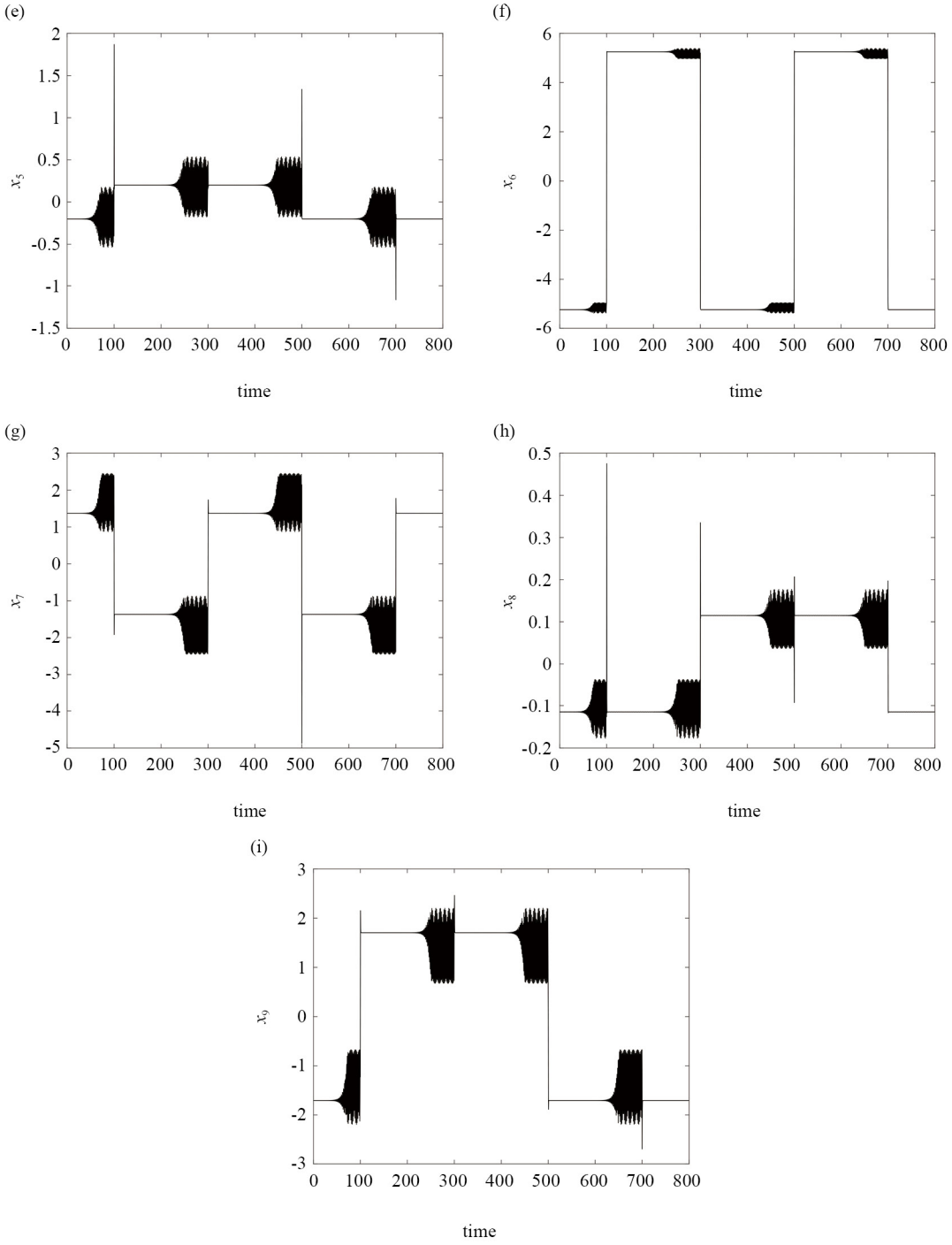

Figure 12. The states x_i $(i = 1, \ldots, 9)$ versus time at $R_e = 19$ when the controllers are switched on and off over the time interval $t \in [0, 800]$ and when the desired fixed point x_d is one of the four unstable fixed points

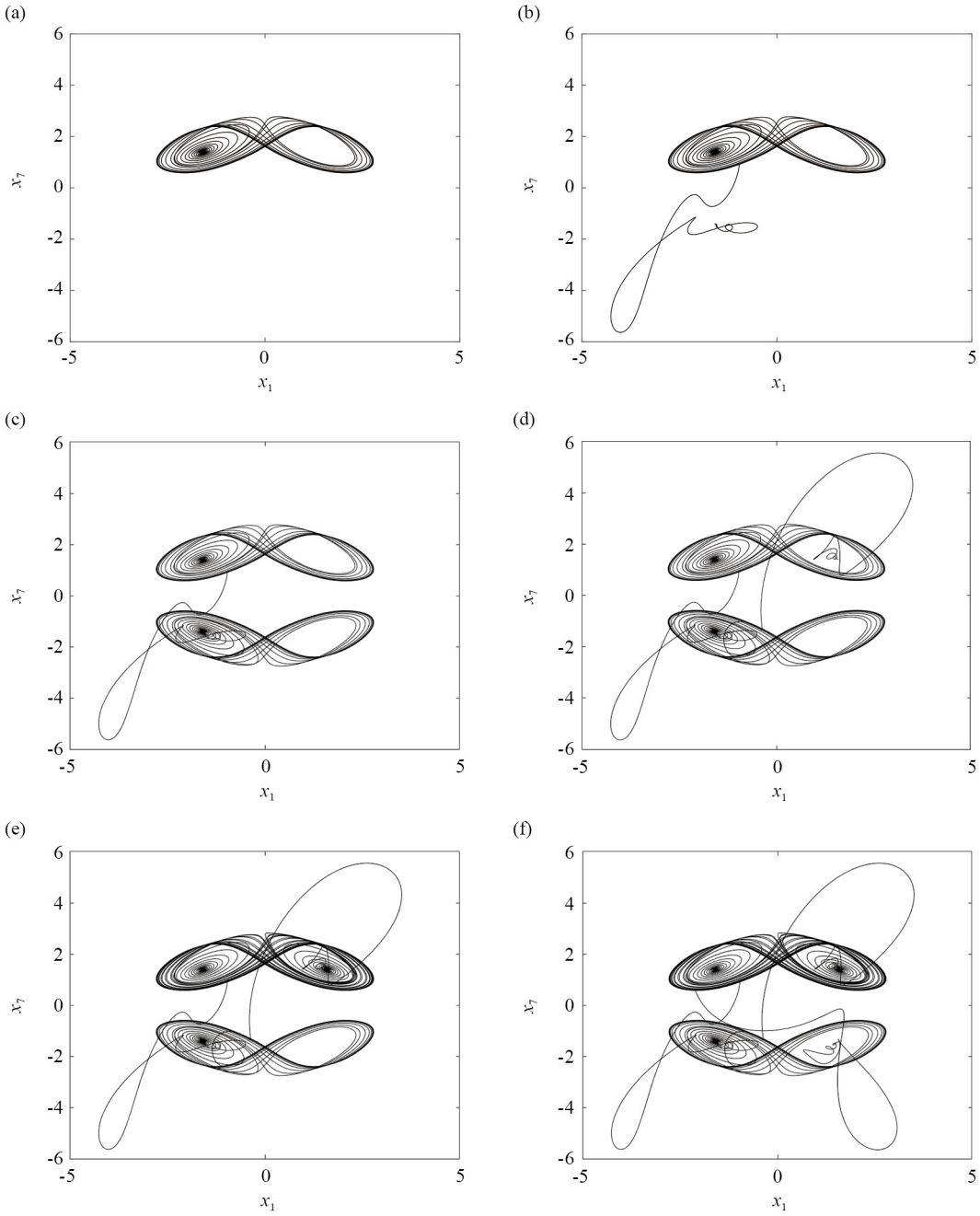
(a)
(b)
(c)
(d)
(e)
(f)
x_7
x_1
6
4
2
0
-2
-4
-6
-5
0
5

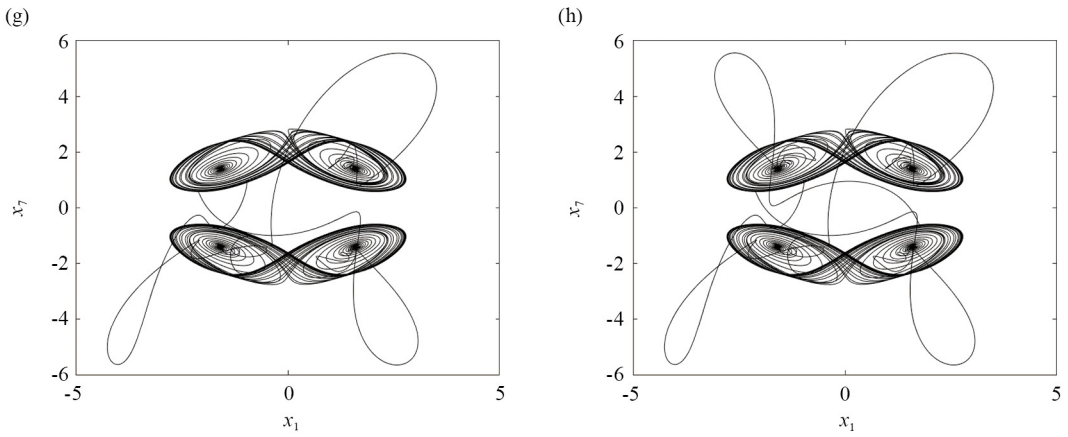

Figure 13. Phase portraits of the controlled and uncontrolled dynamics at $R_e = 21$, showing $x_7(t)$ versus $x_1(t)$ over the time interval $t \in [0,\ 800]$. Subfigures (a), (c), (e), and (g) correspond to intervals where the control is switched off, resulting in transitions between distinct stable periodic orbits. Subfigures (b), (d), (f), and (h) show the controlled dynamics, during which the system is driven toward specific target states X_{2d}, X_{3d}, X_{4d}, and X_{1d}, respectively. The cyclic switching highlights the controller's ability to steer the system between coexisting attractors

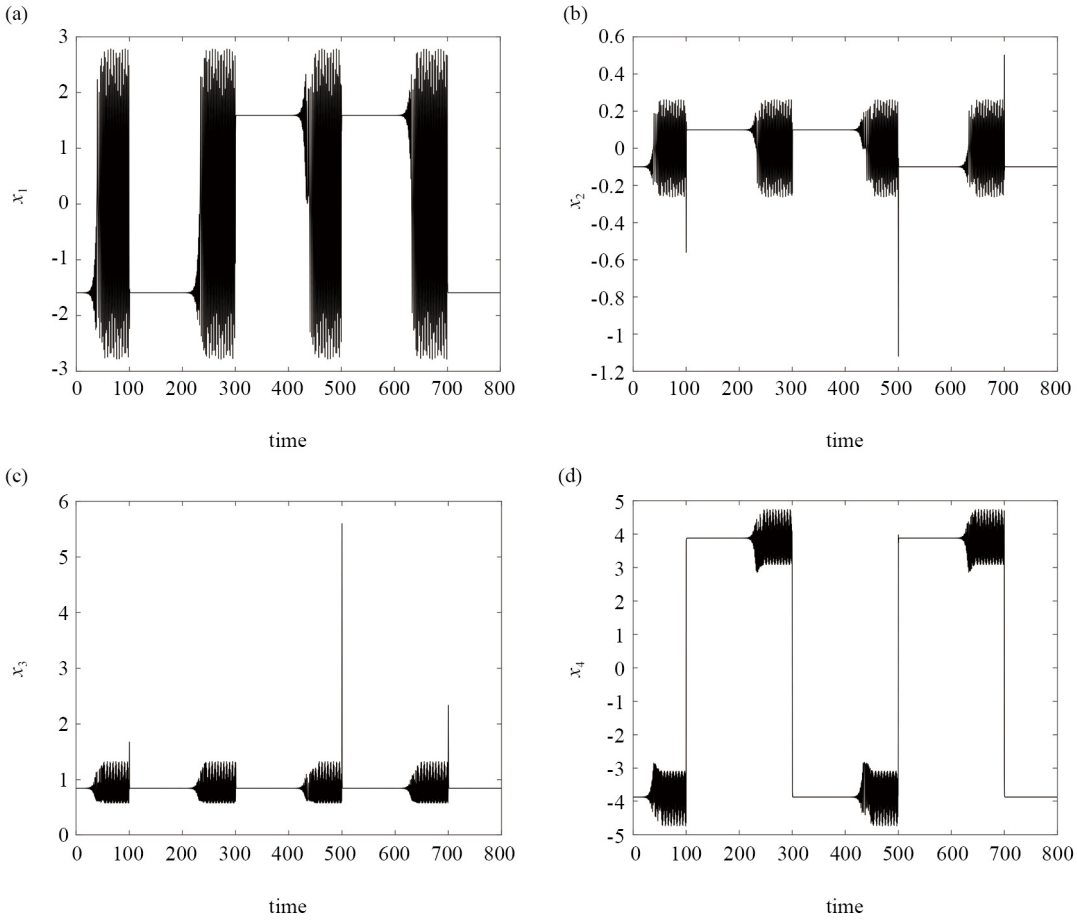

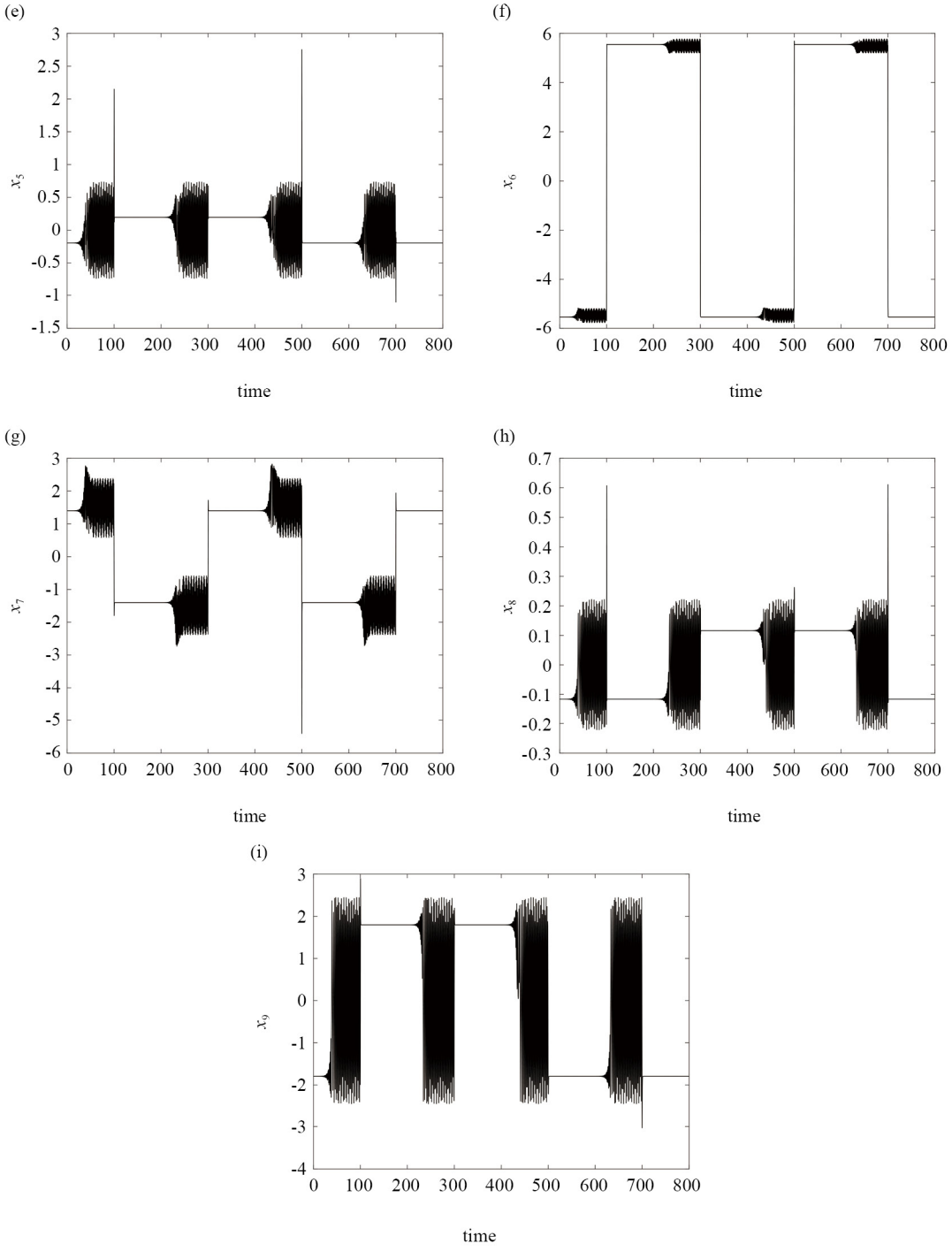

Figure 14. The states $x_i\,(i = 1,\ ...,\ 9)$ versus time at $R_e = 21$ when the controllers are switched on and off over the time interval $t \in [0,\ 800]$ and when the desired fixed point x_d is one of the four unstable fixed points

The simulation results for $R_e = 21$ are shown in Figures 13 and 14. Figure 13 presents the phase portrait of the controlled states $x_7(t)$ versus $x_1(t)$ as the control is switched on and off over $t \in [0,\ 800]$. Specifically:

• Figure 13a shows the uncontrolled dynamics for $t \in [0,\ 100]$, resulting in the first stable periodic orbit.

• Figure 13b illustrates the controlled dynamics for $t \in [100.001,\ 200]$, where the states $x_i(t)$, $i = 1,\ \ldots,\ 9$, converge to X_{2d}.

• In Figure 13c, the control is switched off for $t \in [200.001,\ 300]$, producing the second stable periodic orbit.

• Figure 13d displays the system behavior under control for $t \in [300.001,\ 400]$, leading to convergence toward X_{3d}.

• Figure 13e captures the uncontrolled dynamics for $t \in [400.001,\ 500]$, with the trajectory returning to the first periodic orbit, now approached from the opposite direction.

• Figure 13f shows the controlled dynamics for $t \in [500.001,\ 600]$, where the states converge to X_{4d}.

• In Figure 13g, the control is again switched off for $t \in [600.001,\ 700]$, guiding the system back to the second periodic orbit from the opposite side.

• Finally, Figure 13h illustrates the controlled behavior for $t \in [700.001,\ 800]$, where the states converge to X_{1d}.

Figure 14 shows the time evolution of the controlled states $x_i(t)$, for $i = 1,\ \ldots,\ 9$, clearly depicting the transitions between periodic behaviors when the control is off and convergence to the desired fixed points when the control is active.

These figures demonstrate how the system's states $x_i(t)$ reliably converge to the desired fixed points under control, and return to the system's two stable periodic attractors when the control is deactivated.

4. Control of the dynamics of the reduced-order model to periodic orbits or chaotic states

In this section, a Lyapunov-based controller is designed to regulate the dynamics of the reduced-order model toward periodic or chaotic states. The proposed approach involves synchronizing two ODE systems derived from the two-dimensional Navier-Stokes equations using a truncated Fourier expansion, with either identical or different Reynolds numbers (See Appendix A. 2 for the controller design).

The closed-loop performance of the slave model (35) driven by the feedback law (39) is assessed in three representative scenarios. Throughout, the feedback gains are fixed at $g_i = 50$ for $i = 1,\ \ldots,\ 4$, whereas the Lyapunov gains are chosen as

$$(b_1,\ b_2,\ b_3,\ b_4,\ b_5,\ b_6,\ b_7,\ b_8,\ b_9) = (1, 7, 1, 3.5, 1, 1, 3, 7.875, 3). \tag{17}$$

All controllers are kept inactive ($u_1 = u_2 = u_3 = u_4 = 0$) during the first 50 s to record the natural evolution; they are then activated at $t = 50$ s to enforce synchronization.

Case I: Periodic-to-periodic synchronization ($R_{e_1} = R_{e_2} = 20$). The master system (34) starts from

$$x(0) = \begin{bmatrix} 0.6950 & 0.0856 & 0.7030 & -2.8728 & 0.2940 & -5.0826 & 2.5914 & 0.0944 & 0.8788 \end{bmatrix}^{\mathsf{T}}, \tag{18}$$

while the slave system (35) is initialized at

$$y(0) = \begin{bmatrix} -2.2422 & 0.1733 & 1.1218 & 4.0664 & 0.3403 & 5.2426 & -1.2645 & -0.1601 & 2.2956 \end{bmatrix}^{\mathsf{T}}. \tag{19}$$

Both states lie on two symmetric periodic orbits. Once the controller is enabled, the slave trajectory is steered onto the master's periodic orbit (identical period and phase), achieving full synchronization.

Case II: Chaotic-to-periodic synchronization ($R_{e_1} = 19$, $R_{e_2} = 20.7$). The master system is initialized on a periodic orbit,

$$x(0) = \begin{bmatrix} -1.5582 & 0.1765 & 0.9344 & 3.2309 & 0.5273 & 4.9755 & -2.0371 & -0.1692 & 1.7528 \end{bmatrix}^{\mathsf{T}}, \tag{20}$$

whereas the slave starts on a chaotic attractor,

$$y(0) = \begin{bmatrix} 0.2212 & 0.0265 & 0.6427 & -2.8408 & 0.0928 & -5.1947 & 2.7062 & 0.0310 & 0.3732 \end{bmatrix}^{\mathsf{T}}. \tag{21}$$

After control engagement, the chaotic motion of the slave collapses onto the master's periodic orbit, demonstrating the controller's robustness to both parametric mismatch and initial-condition disparity.

Case III: Chaotic-to-chaotic synchronization ($R_{e_1} = R_{e_2} = 20.7$). Both models share the same Reynolds number but start on distinct chaotic attractors:

$$\begin{aligned} x(0) &= \begin{bmatrix} -0.2212 & 0.0265 & 0.6427 & 2.8408 & 0.0928 & 5.1947 & -2.7062 & -0.0310 & 0.3732 \end{bmatrix}^{\mathsf{T}}, \\ y(0) &= \begin{bmatrix} 0.2212 & 0.0265 & 0.6427 & -2.8408 & 0.0928 & -5.1947 & 2.7062 & 0.0310 & 0.3732 \end{bmatrix}^{\mathsf{T}}. \end{aligned} \tag{22}$$

Upon activation, the slave trajectory is driven from its initial chaotic attractor to the master's target chaotic set, achieving phase-space synchronization despite the complex structure of the attractors.

In all three scenarios, the synchronization error $\|\xi(t)\|$ decays monotonically to zero after controller activation, thus providing numerical evidence in support of the convergence properties established earlier.

Figure 15 summarizes Case I. Figure 15 illustrates the effectiveness of the Lyapunov-based control strategy in synchronizing a slave system to a symmetrized periodic orbit exhibited by the master system at $R_e = 20$. Figure 15a displays the phase portrait of the master system, capturing the periodic trajectory in the (x_1, x_7)-plane, while Figure 15b shows the corresponding time evolution of $x_1(t)$. After the control is activated at $t = 50$, the slave system begins to synchronize, as evidenced by the phase portrait in Figure 15c and the time evolution in Figure 15d. Figures 15e and 15f confirm the convergence of the slave trajectory to the master trajectory in both phase space and time. Finally, Figure 15g shows the evolution of the L_2-norm of the error, $\|\mathbf{e}(t)\|$,

$$\|\mathbf{e}(t)\|_2 = \left(\sum_{i=1}^{9} |x_i(t) - y_i(t)|^2\right)^{1/2}, \tag{23}$$

which decays to zero as $t \to \infty$, demonstrating successful synchronization and control convergence.

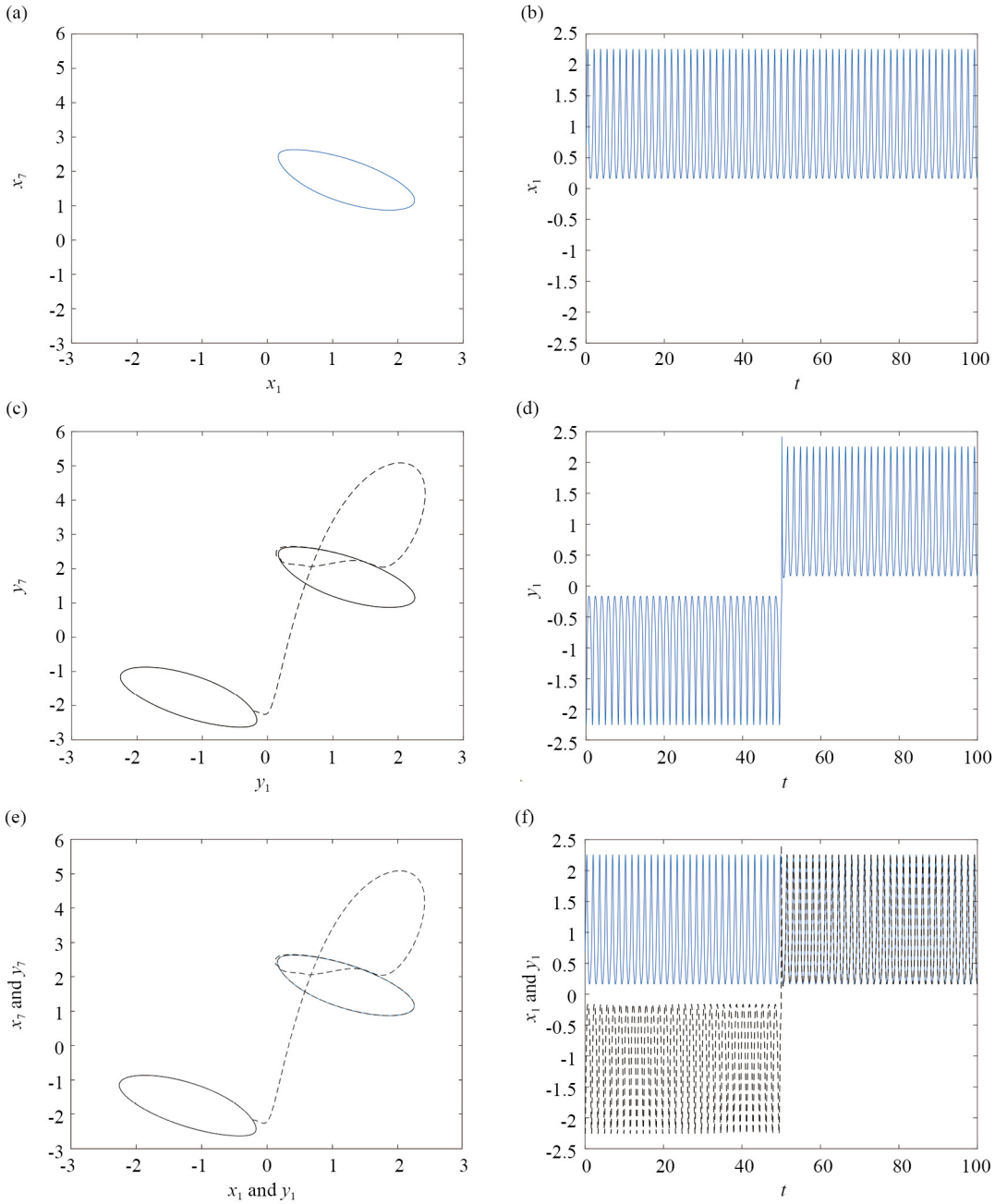
(a)
x_7
x_1
(b)
x_1
t
(c)
y_7
y_1
(d)
y_1
t
(e)
x_7 and y_7
x_1 and y_1
(f)
x_1 and y_1
t

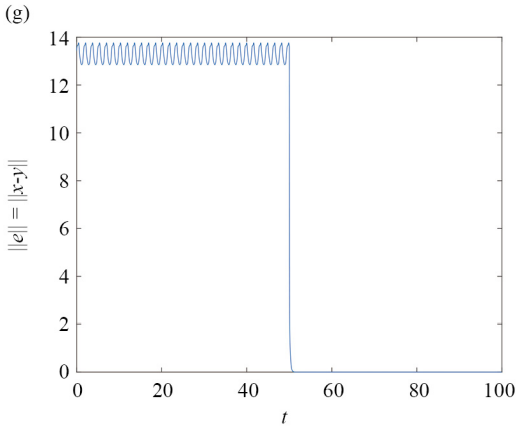

Figure 15. Lyapunov control of a periodic orbit to a symmetrized periodic orbit when both the slave and the master system have the same Reynolds number R_e =20. The control is switched on at t = 50. (a) Phase portrait of the master system showing $x_7(t)$ versus $x_1(t)$. (b) Time evolution of $x_1(t)$ of the master system. (c) Phase portrait of the slave system showing $y_7(t)$ versus $y_1(t)$ after control activation. (d) Time evolution of $y_1(t)$ of the slave system. (e) Phase portrait of $x_7(t)$ and $y_7(t)$ versus $x_1(t)$ and $y_1(t)$. (f) Time evolution of $x_1(t)$ and $y_1(t)$, showing convergence. (g) Evolution of the L_2-norm error $\|\mathbf{e}\|$, demonstrating that the error converges to zero as $t \to \infty$

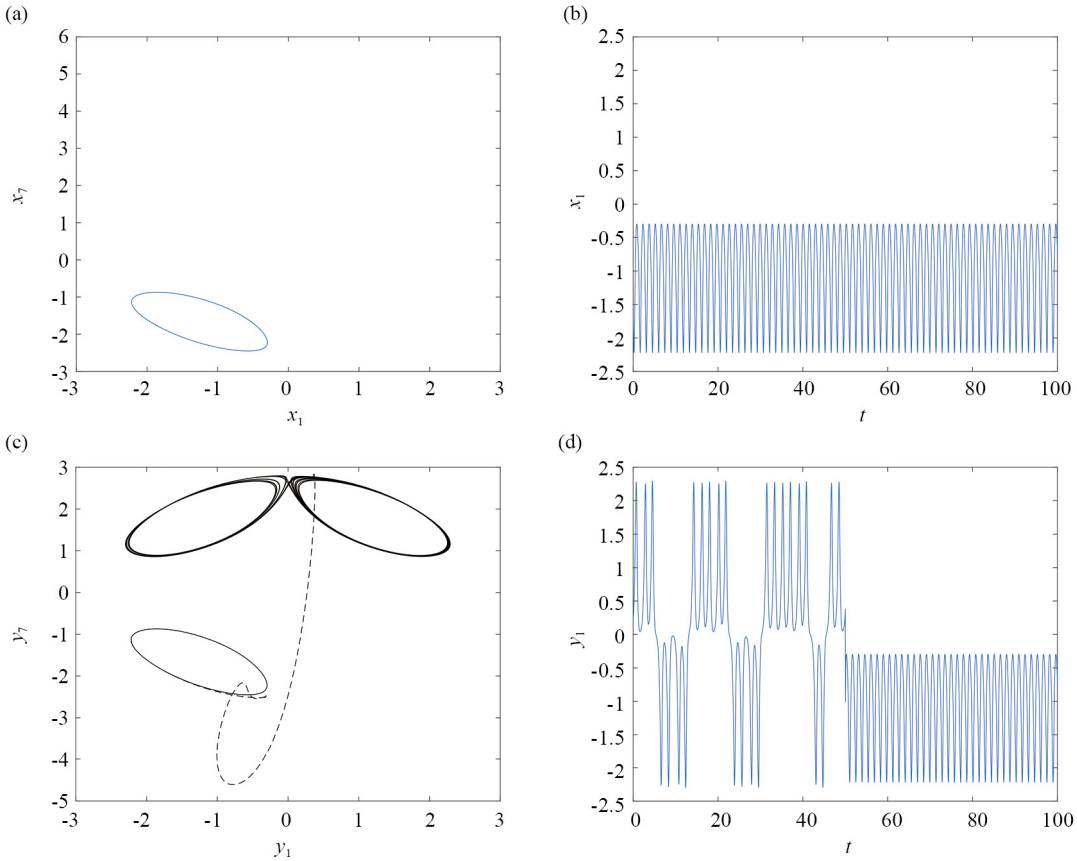

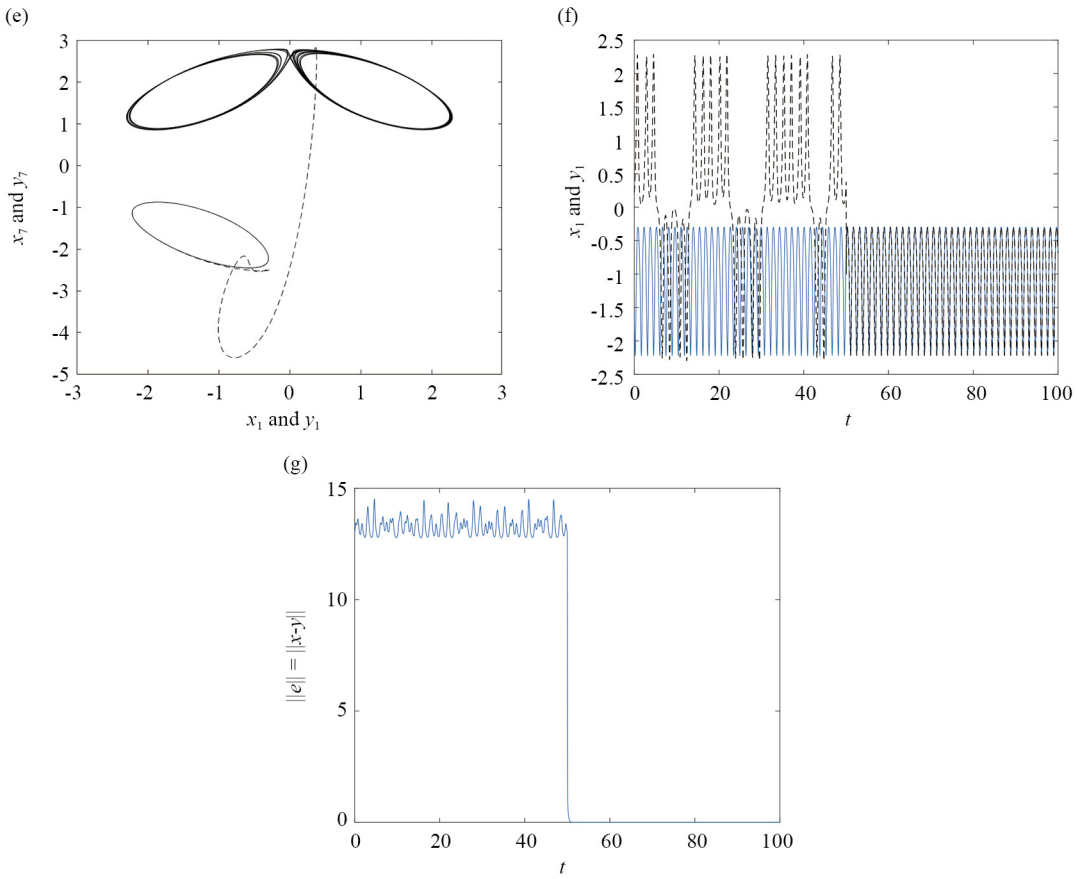

Figure 16. Control of a chaotic attractor to a periodic orbit when $R_e = 20.7$ in the slave system and $R_e = 19$ in the master system. The control is switched on at $t = 50$. (a) Phase portrait of the master system showing $x_7(t)$ versus $x_1(t)$. (b) Time evolution of $x_1(t)$ of the master system. (c) Phase portrait of the slave system showing $y_7(t)$ versus $y_1(t)$ after control activation. (d) Time evolution of $y_1(t)$ of the slave system. (e) Phase portrait of $x_7(t)$ and $y_7(t)$ versus $x_1(t)$ and $y_1(t)$. (f) Time evolution of $x_1(t)$ and $y_1(t)$, showing convergence. (g) Evolution of the L_2-norm error $\|\mathbf{e}\|$, demonstrating that the error converges to zero as $t \to \infty$

Figures 16 and 17 provide analogous results for Cases II and III, respectively. That is, Figure 16 demonstrates the application of the Lyapunov-based control strategy to synchronize a slave system exhibiting chaotic behavior at $R_e = 20.7$ with a master system evolving on a periodic orbit at $R_e = 19$. Figure 16a presents the phase portrait of the master system in the (x_1, x_7)-plane, highlighting its periodic nature, while Figure 16b displays the corresponding time evolution of $x_1(t)$. After the control is activated at $t = 50$, the chaotic dynamics of the slave system begin to transition toward the periodic behavior of the master, as seen in the phase portrait of Figure 16c and the time series in Figure 16d. The synchronization process is further illustrated in Figure 16e, which shows the joint evolution of both systems in phase space, and Figure 16f, which confirms the convergence of the slave's trajectory to that of the master in time. Figure 16g plots the evolution of the L_2-norm of the synchronization error, $\|\mathbf{e}(t)\|$, which tends to zero as $t \to \infty$, confirming the effectiveness of the control scheme in stabilizing chaotic behavior to a desired periodic orbit.

On the other hand, Figure 17 presents the synchronization of two chaotic attractors using the Lyapunov-based control approach, where both the master and slave systems operate at $R_e = 20.7$. The master system evolves on a specific chaotic attractor, as illustrated by the phase portrait in Figure 17a and the corresponding time evolution of $x_1(t)$ in Figure 17b. After the control is switched on at $t = 50$, the slave system begins to transition from its initial chaotic trajectory to match the target chaotic dynamics of the master. This transition is visualized in Figure 17c through the phase portrait of the slave system and in Figure 17d via the time series of $y_1(t)$. The synchronization process is further confirmed by the joint phase

portrait in Figure 17e and the overlapping time histories in Figure 17f, which show the convergence of the slave trajectory to that of the master. Finally, Figure 17g displays the evolution of the L_2-norm of the synchronization error, $\|\mathbf{e}(t)\|$, which decreases to zero as $t \to \infty$, demonstrating successful synchronization between two distinct chaotic attractors.

In every scenario, the error norm $\|\mathbf{e}(t)\|_2$ decays monotonically to zero once the control is enabled, confirming that the feedback law (39) successfully synchronizes the master (34) and slave (35) models irrespective of Reynolds-number mismatch or disparate initial conditions.

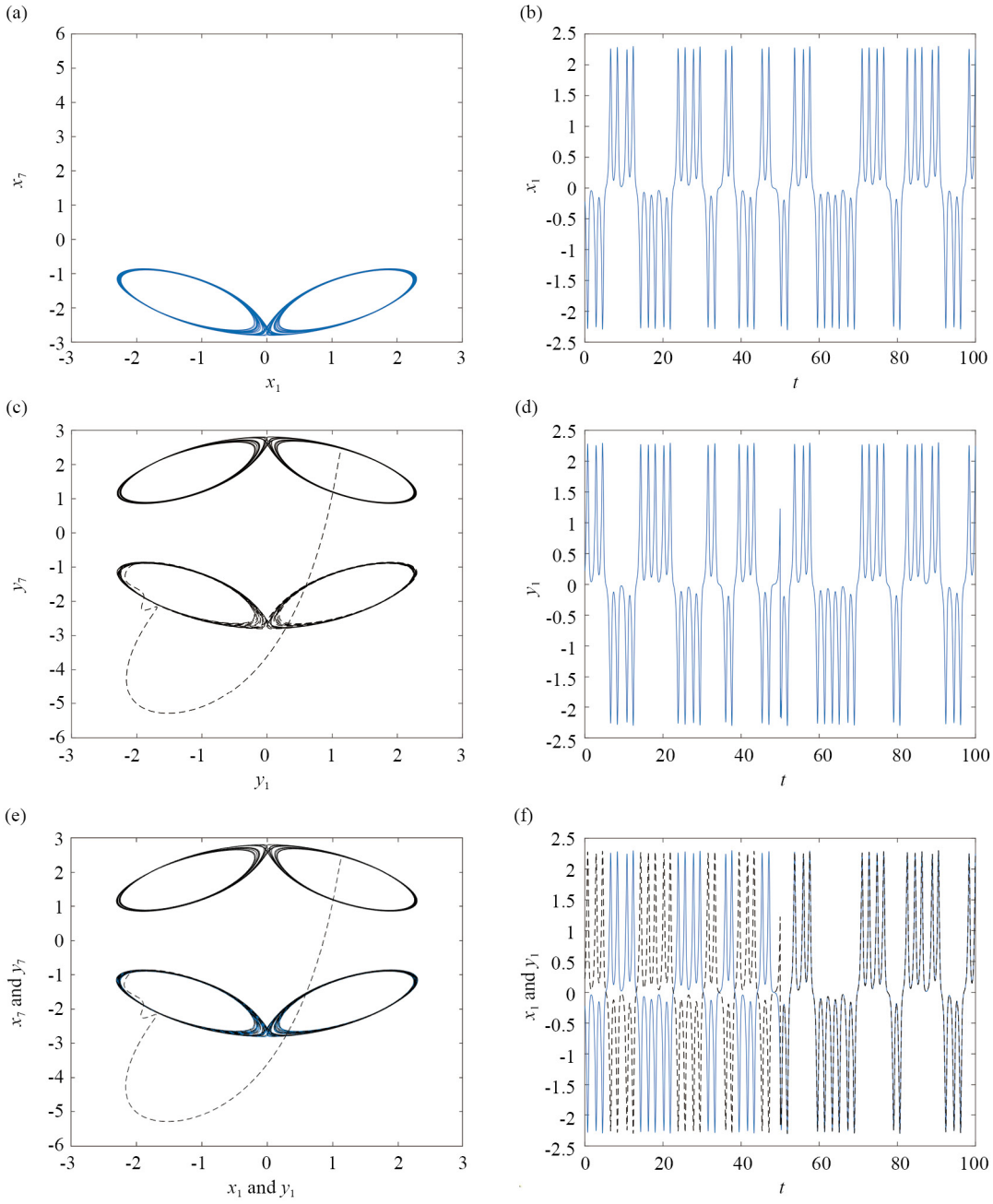

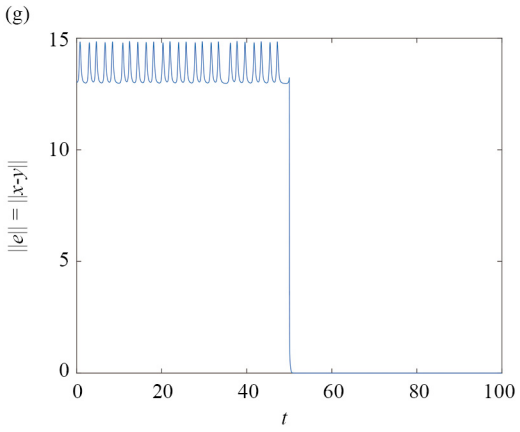

Figure 17. Control of a chaotic attractor to a different chaotic attractor when $R_e = 20.7$ in both the slave system and the master system. The control is switched on at t = 50. (a) Phase portrait of the master system showing $x_7(t)$ versus $x_1(t)$. (b) Time evolution of $x_1(t)$ of the master system. (c) Phase portrait of the slave system showing $y_7(t)$ versus $y_1(t)$ after control activation. (d) Time evolution of $y_1(t)$ of the slave system. (e) Phase portrait of $x_7(t)$ and $y_7(t)$ versus $x_1(t)$ and $y_1(t)$. (f) Time evolution of $x_1(t)$ and $y_1(t)$, showing convergence. (g) Evolution of the L_2-norm error $\|\mathbf{e}\|$, demonstrating that the error converges to zero as $t \to \infty$

5. Concluding remarks

This study investigated the dynamics and control of the two-dimensional Kolmogorov flow using a reduced-order model derived from the two-dimensional Navier-Stokes equations via the Fourier-Galerkin method. The resulting nine-dimensional system of nonlinear ODEs successfully reproduced key features of the original flow, including steady states, periodic orbits, and chaotic attractors across a range of Reynolds numbers $0 < R_e < 30$. To regulate the system, we developed a Lyapunov-based controller. Numerical simulations demonstrated the effectiveness of the proposed controller in driving the system toward desired fixed points, periodic solutions or chaotic attractors while ensuring robustness against nonlinearities and dynamic transitions. Overall, the results highlight the potential of combining reduced-order modeling with nonlinear control techniques to effectively manage and stabilize complex fluid flows, with promising applicability to more realistic three-dimensional Navier-Stokes systems and other nonlinear high-dimensional dynamical models.

Author contribution

N.S.: Conceptualization, Methodology, Visualization, Formal analysis, Data Curation, Software, Writing-Original draft; Writing-Review and Editing, Supervision N.E.: Formal analysis, Data Curation, Software, Writing-Review and Editing M.Z.: Formal analysis, Writing-Review and Editing.

Confilict of interest

The authors declare that they have no conflict of interest.

References

[1] Arnol'd VL, Mechalkin LD. A. N. Kolmogorov's seminar on selected problems of analysis (1958/1959). *Russian Mathematical Surveys*. 1960; 15(1): 247-250.

[2] Smaoui N, Al-Yakoob SM. Analyzing the dynamics of cellular flames using Karhunen-Loeve decomposition and autoassociative neural networks. *SIAM Journal on Scientific Computing*. 2003; 24(5): 1790-1808. Available from: https://doi.org/10.1137/S1064827501386201.

[3] Smaoui N. Artificial neural network-based low-dimensional model for spatio-temporally varying cellular flames. *Applied Mathematical Modelling*. 1997; 21(12): 739-748. Available from: https://doi.org/10.1016/S0307-904X(97)00092-9.

[4] Smaoui N. Linear versus nonlinear dimensionality reduction of high-dimensionla dynamical systems. *SIAM Journal on Scientific Computing*. 2004; 25(6): 2107-2125. Available from: https://doi.org/10.1137/S1064827502412723.

[5] De Jesús CEP, Graham MD. Data-driven low-dimensional dynamic model of Kolmogorov flow. *Physical Review Fluids*. 2023; 8(4): 044402. Available from: https://doi.org/10.1103/PhysRevFluids.8.044402.

[6] Feudel F, Seehafer N. Bifurcations and pattern formation in a two-dimensional Navier-Stokes fluid. *Physical Review E*. 1995; 52(4): 3506. Available from: https://doi.org/10.1103/PhysRevE.52.3506.

[7] Armbruster D, Nicolaenko B, Smaoui N, Chossat P. Symmetries and dynamics for 2-d Navier-Stokes flow. *Physica D: Nonlinear Phenomena*. 1996; 95(1): 81-93. Available from: https://doi.org/10.1016/0167-2789(96)00006-1.

[8] Boldrighini C, Franceschini V. A five-dimensional truncation of the plane incompressible Navier-Stokes equations. *Communications in Mathematical Physics*. 1979; 64: 159-170. Available from: https://doi.org/10.1016/0167-2789(96)00006-1.

[9] Braun R, Feudel F, Guzdar P. Route to chaos for a two-dimensional externally driven flow. *Physical Review E*. 1998; 58(2): 1927. Available from: https://doi.org/10.1103/PhysRevE.58.1927.

[10] Chen Z-M, Price WG. Time dependent periodic Navier-Stokes flows on a two-dimensional torus. *Communications in Mathematical Physics*. 1996; 179(3): 577-597. Available from: https://doi.org/10.1007/BF02100098.

[11] Chen Z-M, Price WG. Transition to chaos in a fluid motion system. *Chaos, Solitons and Fractals*. 2005; 26(4): 1195-1202. Available from: https://doi.org/10.1016/j.chaos.2005.02.045.

[12] Franceschini V, Tebaldi C. A seven-mode truncation of the plane incompressible Navier-Stokes equations. *Journal of Statistical Physics*. 1981; 25: 397-417. Available from: https://doi.org/10.1007/BF01010796.

[13] Franceschini V, Tebaldi C. Sequences of infinite bifurcations and turbulence in a five-mode truncation of the Navier-Stokes equations. *Journal of Statistical Physics*. 1979; 21(6): 707-726. Available from: https://doi.org/10.1007/BF01107910.

[14] Smaoui N, Armbruster D. Symmetry and the Karhunen-Loeve analysis. *SIAM Journal on Scientific Computing*. 1997; 18(5): 1526-1532. Available from: https://doi.org/10.1137/S1064827596309694.

[15] Smaoui N. Symmetries, dynamics, and control for the 2d Kolmogorov flow. *Complexity*. 2018; 2018(1): 4602485. Available from: https://doi.org/10.1155/2018/4602485.

[16] Smaoui N, El-Kadri A, Zribi M. On the control of the 2d Navier-Stokes equations with Kolmogorov forcing. *Complexity*. 2021; 2021(1): 3912014. Available from: https://doi.org/10.1155/2021/3912014.

[17] Smaoui N, Zribi M. Dynamics and control of the 2-d Navier-Stokes equations. *Applied Mathematics and Computation*. 2014; 237: 461-473. Available from: https://doi.org/10.1016/j.amc.2014.03.150.

[18] Smaoui N, Zribi M. Dynamics and control of the seven-mode truncation system of the 2-d Navier-Stokes equations. *Communications in Nonlinear Science and Numerical Simulation*. 2016; 32: 169-189. Available from: https://doi.org/10.1016/j.cnsns.2015.08.012.

[19] Smaoui N, Zribi M. On the control of the chaotic attractors of the 2-d Navier-Stokes equations. *Chaos: An Interdisciplinary Journal of Nonlinear Science*. 2017; 27(3): 033111. Available from: https://doi.org/10.1063/1.4978682.

[20] Feudel F, Seehafer N. On the bifurcation phenomena in truncation of the 2D Navier-Stokes equations. *Chaos, Solitons and Fractals*. 1995; 5(10): 1805-1816. Available from: https://doi.org/10.1016/0960-0779(94)00190-2.

[21] Smaoui N, El-Khadri A, Zribi M. Nonlinear boundary control of the unforced generalized Korteweg-de Vries-Burgers equation. *Nonlinear Dynamics*. 2010; 60(4): 561-574. Available from: https://doi.org/10.1007/s11071-009-9615-8.

[22] Nicolis C, Nicolis G. Energy dissipation and dynamical complexity in a truncated two-dimensional Navier-Stokes dynamics. *Physica D: Nonlinear Phenomena*. 2001; 155(3-4): 184-200. Available from: https://doi.org/10.1016/S0167-2789(01)00258-5.

[23] Guan S, Zhou YC, Wei GW, Lai C-H. Controlling flow turbulence. *Chaos: An Interdisciplinary Journal of Nonlinear Science*. 2003; 13(1): 64-70. Available from: https://doi.org/10.1063/1.1539017.

[24] Gambino G, Lombardo MC, Sammartino M. Adaptive control of a seven mode truncation of the Kolmogorov flow with drag. *Chaos, Solitons and Fractals*. 2009; 41(1): 47-59. Available from: https://doi.org/10.1016/j.chaos.2007.11.003.

[25] Musacchio S, Boffetta G. Turbulent channel without boundaries: The periodic Kolmogorov flow. *Physical Review E*. 2014; 89(2): 023004. Available from: https://doi.org/10.1103/PhysRevE.89.023004.

[26] Suri B, Tithof J, Mitchell R, Grigoriev RO, Schatz MF. Velocity profile in a two-layer Kolmogorov-like flow. *Physics of Fluids*. 2014; 26(5): 053601. Available from: https://doi.org/10.1063/1.4873417.

[27] Mishra PK, Herault J, Fauve S, Verma MK. Dynamics of reversals and condensates in two-dimensional Kolmogorov flows. *Physical Review E*. 2015; 91(5): 053005. Available from: https://doi.org/10.1103/PhysRevE.91.053005.

[28] Tithof J, Suri B, Pallantla RV, Grigoriev RO, Schatz MF. Bifurcations in a quasi-two-dimensional Kolmogorov-like flow. *Journal of Fluid Mechanics*. 2017; 828: 837-866. Available from: https://doi.org/10.1017/jfm.2017.553.

[29] Fylladitakis E. Kolmogorov flow: Seven decades of history. *Journal of Applied Mathematics and Physics*. 2018; 6(11): 2227. Available from: https://doi.org/10.4236/jamp.2018.611187.

Appendix A

A.1 *Controller design for driving the dynamics of the reduced-order model to a fixed point*

In this section, we develop a Lyapunov-based controller to drive the system states toward a specified fixed point, regardless of its stability.

The control inputs are incorporated into the first, third, fifth, and sixth equations of system (6), yielding the following system:

$$\begin{aligned}
\dot{x}_1 &= -2x_1 + 4x_2x_7 - 3\sqrt{2}x_3x_8 - 4x_4x_5 + u_1,\\
\dot{x}_2 &= -9x_2 + 3x_1x_7 + 9x_6x_8,\\
\dot{x}_3 &= -4x_3 + 4\sqrt{2}x_1x_8 + 4\sqrt{2}x_6x_7 - 4\sqrt{2}x_4x_6 + 8R_e + u_2,\\
\dot{x}_4 &= -5x_4 + x_1x_5 + 3\sqrt{2}x_3x_6 - \frac{9\sqrt{5}}{5}x_5x_8,\\
\dot{x}_5 &= -x_5 + 3x_1x_4 - \sqrt{5}x_1x_6 + \sqrt{5}x_4x_8 + u_3,\\
\dot{x}_6 &= -x_6 + \sqrt{5}x_1x_5 - x_2x_8 + \sqrt{2}x_3x_4 - \sqrt{2}x_3x_7 + u_4,\\
\dot{x}_7 &= -5x_7 - 7x_1x_2 - \frac{9\sqrt{5}}{5}x_1x_9 - 3\sqrt{2}x_3x_6,\\
\dot{x}_8 &= -10x_8 - \sqrt{2}x_1x_3 - 8x_2x_6 + \frac{4\sqrt{5}}{5}x_4x_5,\\
\dot{x}_9 &= -5x_9 + \frac{9\sqrt{5}}{5}x_1x_7.
\end{aligned} \tag{24}$$

Let $x_d = \begin{bmatrix} x_{1d} & x_{2d} & x_{3d} & x_{4d} & x_{5d} & x_{6d} & x_{7d} & x_{8d} & x_{9d} \end{bmatrix}^T$ denote the constant desired fixed point. An equilibrium point of system (24) must satisfy the following algebraic equations:

$$-9x_{2d} + 3x_{1d}x_{7d} + 9x_{6d}x_{8d} = 0,$$

$$-5x_{4d} + x_{1d}x_{5d} + 3\sqrt{2}x_{3d}x_{6d} - \frac{9\sqrt{5}}{5}x_{5d}x_{8d} = 0,$$

$$-5x_{7d} - 7x_{1d}x_{2d} - \frac{9\sqrt{5}}{5}x_{1d}x_{9d} - 3\sqrt{2}x_{3d}x_{6d} = 0,$$

$$
\begin{aligned}
&-10x_{8d}-\sqrt{2}x_{1d}x_{3d}-8x_{2d}x_{6d}+\frac{4\sqrt{5}}{5}x_{4d}x_{5d}=0,\\
&-5x_{9d}+\frac{9\sqrt{5}}{5}x_{1d}x_{7d}=0.
\end{aligned}
\tag{25}
$$

Define the errors $\xi_i(i=1,\ ...,\ 9)$ such that

$$
\begin{aligned}
\xi_1&=x_1-x_{1d},\\
\xi_2&=x_2-x_{2d},\\
\xi_3&=x_3-x_{3d},\\
\xi_4&=x_4-x_{4d},\\
\xi_5&=x_5-x_{5d},\\
\xi_6&=x_6-x_{6d},\\
\xi_7&=x_7-x_{7d},\\
\xi_8&=x_8-x_{8d},\\
\xi_9&=x_9-x_{9d}.
\end{aligned}
\tag{26}
$$

Using equations (24), (25) and (26), we can obtain the error ODE system as follows:

$$
\begin{aligned}
\dot{\xi}_1=&-2\xi_1-4\xi_4\xi_5-4x_{5d}\xi_4-4x_{4d}\xi_5+4\xi_2\xi_7+4x_{7d}\xi_2+4x_{2d}\xi_7\\
&-3\sqrt{2}\xi_3\xi_8-3\sqrt{2}x_{8d}\xi_3-3\sqrt{2}x_{3d}\xi_8+m_1+u_1,\\
\dot{\xi}_2=&-9\xi_2+3\xi_1\xi_7+3x_{7d}\xi_1+3x_{1d}\xi_7+9\xi_6\xi_8+9x_{8d}\xi_6+9x_{6d}\xi_8,\\
\dot{\xi}_3=&-4\xi_3+4\sqrt{2}\xi_1\xi_8+4\sqrt{2}x_{8d}\xi_1+4\sqrt{2}x_{1d}\xi_8+4\sqrt{2}\xi_6\xi_7+4\sqrt{2}x_{7d}\xi_6+4\sqrt{2}x_{6d}\xi_7\\
&-4\sqrt{2}\xi_4\xi_6-4\sqrt{2}x_{6d}\xi_4-4\sqrt{2}x_{4d}\xi_6+m_2+u_2,
\end{aligned}
$$

$$
\begin{aligned}
\dot{\xi}_4 =& -5\xi_4 + \xi_1\xi_5 + x_{5d}\xi_1 + x_{1d}\xi_5 + 3\sqrt{2}\xi_3\xi_6 + 3\sqrt{2}x_{6d}\xi_3 + 3\sqrt{2}x_{3d}\xi_6 \\
& - \frac{9\sqrt{5}}{5}\xi_5\xi_8 - \frac{9\sqrt{5}}{5}x_{8d}\xi_5 - \frac{9\sqrt{5}}{5}x_{5d}\xi_8, \\
\dot{\xi}_5 =& -\xi_5 + 3\xi_1\xi_4 + 3x_{4d}\xi_1 + 3x_{1d}\xi_4 - \sqrt{5}\xi_1\xi_6 - \sqrt{5}x_{6d}\xi_1 - \sqrt{5}x_{1d}\xi_6 \\
& + \sqrt{5}\xi_4\xi_8 + \sqrt{5}x_{8d}\xi_4 + \sqrt{5}x_{4d}\xi_8 + m_3 + u_3, \\
\dot{\xi}_6 =& -\xi_6 + \sqrt{5}\xi_1\xi_5 + \sqrt{5}x_{5d}\xi_1 + \sqrt{5}x_{1d}\xi_5 - \xi_2\xi_8 - x_{8d}\xi_2 - x_{2d}\xi_8 + \sqrt{2}\xi_3\xi_4 \\
& + \sqrt{2}x_{4d}\xi_3 + \sqrt{2}x_{3d}\xi_4 - \sqrt{2}\xi_3\xi_7 - \sqrt{2}x_{7d}\xi_3 - \sqrt{2}x_{3d}\xi_7 + m_4 + u_4, \\
\dot{\xi}_7 =& -5\xi_7 - 7\xi_1\xi_2 - 7x_{2d}\xi_1 - 7x_{1d}\xi_2 - \frac{9\sqrt{5}}{5}\xi_1\xi_9 - \frac{9\sqrt{5}}{5}x_{9d}\xi_1 - \frac{9\sqrt{5}}{5}x_{1d}\xi_9 - 3\sqrt{2}\xi_3\xi_6 \\
& - 3\sqrt{2}x_{6d}\xi_3 - 3\sqrt{2}x_{3d}\xi_6, \\
\dot{\xi}_8 =& -10\xi_8 - \sqrt{2}\xi_1\xi_3 - \sqrt{2}x_{3d}\xi_1 - \sqrt{2}x_{1d}\xi_3 - 8\xi_2\xi_6 - 8x_{6d}\xi_2 - 8x_{2d}\xi_6 \\
& + \frac{4\sqrt{5}}{5}\xi_4\xi_5 + \frac{4\sqrt{5}}{5}x_{5d}\xi_4 + \frac{4\sqrt{5}}{5}x_{4d}\xi_5, \\
\dot{\xi}_9 =& -5\xi_9 + \frac{9\sqrt{5}}{5}\xi_1\xi_7 + \frac{9\sqrt{5}}{5}x_{7d}\xi_1 + \frac{9\sqrt{5}}{5}x_{1d}\xi_7.
\end{aligned}
\tag{27}
$$

Where the parameters m_1, m_2, m_3 and m_4 are defined such that:

$$
\begin{aligned}
m_1 &= -2x_{1d} + 4x_{2d}x_{7d} - 3\sqrt{2}x_{3d}x_{8d} - 4x_{4d}x_{5d}, \\
m_2 &= -4x_{3d} + 4\sqrt{2}x_{1d}x_{8d} + 4\sqrt{2}x_{6d}x_{7d} - 4\sqrt{2}x_{4d}x_{6d} + 8R_e, \\
m_3 &= -x_{5d} + 3x_{1d}x_{4d} - \sqrt{5}x_{1d}x_{6d} + \sqrt{5}x_{4d}x_{8d}, \\
m_4 &= -x_{6d} + \sqrt{5}x_{1d}x_{5d} - x_{2d}x_{8d} + \sqrt{2}x_{3d}x_{4d} - \sqrt{2}x_{3d}x_{7d}.
\end{aligned}
\tag{28}
$$

A.1.1 *Lyapunov-based control*

Let the control gains a_i, $(i = 1, \ldots, 9)$ be positive scalars such that:

$$
\begin{aligned}
&3a_2 - 7a_7 = 0,\\
&9a_2 - 8a_8 = 0,\\
&-9a_4 + 4a_8 = 0,\\
&-a_7 + a_9 = 0.
\end{aligned}
\tag{29}
$$

Also, let c_1, c_2, c_3, c_4 be positive design parameters.

Theorem 1 The control law,

$$
\begin{aligned}
u_1 = {} & 4\xi_4\xi_5 + 4x_{5d}\xi_4 + 4x_{4d}\xi_5 - 4\xi_2\xi_7 - 4x_{7d}\xi_2 - 4x_{2d}\xi_7 + 3\sqrt{2}\xi_3\xi_8 + 3\sqrt{2}x_{8d}\xi_3\\
& + 3\sqrt{2}x_{3d}\xi_8 - 3\frac{a_2}{a_1}\xi_2\xi_7 - 3\frac{a_2}{a_1}x_{7d}\xi_2 - \frac{a_4}{a_1}\xi_4\xi_5 - \frac{a_4}{a_1}x_{5d}\xi_4 + 7\frac{a_7}{a_1}\xi_2\xi_7\\
& + 7\frac{a_7}{a_1}x_{2d}\xi_7 + \frac{9\sqrt{5}}{5}\frac{a_7}{a_1}\xi_7\xi_9 + \frac{9\sqrt{5}}{5}\frac{a_7}{a_1}x_{9d}\xi_7 + \sqrt{2}\frac{a_8}{a_1}\xi_3\xi_8 + \sqrt{2}\frac{a_8}{a_1}x_{3d}\xi_8\\
& - \frac{9\sqrt{5}}{5}\frac{a_9}{a_1}\xi_7\xi_9 - \frac{9\sqrt{5}}{5}\frac{a_9}{a_1}x_{7d}\xi_9 - m_1 - c_1\xi_1,\\
u_2 = {} & -4\sqrt{2}\xi_1\xi_8 - 4\sqrt{2}x_{8d}\xi_1 - 4\sqrt{2}x_{1d}\xi_8 - 4\sqrt{2}\xi_6\xi_7 - 4\sqrt{2}x_{7d}\xi_6 - 4\sqrt{2}x_{6d}\xi_7\\
& + 4\sqrt{2}\xi_4\xi_6 + 4\sqrt{2}x_{6d}\xi_4 + 4\sqrt{2}x_{4d}\xi_6 - 3\sqrt{2}\frac{a_4}{a_3}\xi_4\xi_6 - 3\sqrt{2}\frac{a_4}{a_3}x_{6d}\xi_4\\
& + 3\sqrt{2}\frac{a_7}{a_3}\xi_6\xi_7 + 3\sqrt{2}\frac{a_7}{a_3}x_{6d}\xi_7 + \sqrt{2}\frac{a_8}{a_3}x_{1d}\xi_8 - m_2 - c_2\xi_3,\\
u_3 = {} & -3\xi_1\xi_4 - 3x_{4d}\xi_1 - 3x_{1d}\xi_4 + \sqrt{5}\xi_1\xi_6 + \sqrt{5}x_{6d}\xi_1 + \sqrt{5}x_{1d}\xi_6\\
& - \sqrt{5}\xi_4\xi_8 - \sqrt{5}x_{8d}\xi_4 - \sqrt{5}x_{4d}\xi_8 - \frac{a_4}{a_5}x_{1d}\xi_4 + \frac{9\sqrt{5}}{5}\frac{a_4}{a_5}\xi_4\xi_8\\
& + \frac{9\sqrt{5}}{5}\frac{a_4}{a_5}x_{8d}\xi_4 - \frac{4\sqrt{5}}{5}\frac{a_8}{a_5}\xi_4\xi_8 - \frac{4\sqrt{5}}{5}\frac{a_8}{a_5}x_{4d}\xi_8 - m_3 - c_3\xi_5,
\end{aligned}
$$

$$
\begin{aligned}
u_4 = &-\sqrt{5}\xi_1\xi_5 - \sqrt{5}x_{5d}\xi_1 - \sqrt{5}x_{1d}\xi_5 + \xi_2\xi_8 + x_{8d}\xi_2 + x_{2d}\xi_8 - \sqrt{2}\xi_3\xi_4 \\
&- \sqrt{2}x_{4d}\xi_3 - \sqrt{2}x_{3d}\xi_4 + \sqrt{2}\xi_3\xi_7 + \sqrt{2}x_{7d}\xi_3 + \sqrt{2}x_{3d}\xi_7 - 9\frac{a_2}{a_6}\xi_2\xi_8 - 9\frac{a_2}{a_6}x_{8d}\xi_2 \\
&- 3\sqrt{2}\frac{a_4}{a_6}x_{3d}\xi_4 + 3\sqrt{2}\frac{a_7}{a_6}x_{3d}\xi_7 + 8\frac{a_8}{a_6}\xi_2\xi_8 + 8\frac{a_8}{a_6}x_{2d}\xi_8 - m_4 - c_4\xi_6,
\end{aligned} \tag{30}
$$

when applied to the error system (27), ensures that the error components ξ_i, for $i = 1, \ldots, 9$, decay to zero as $t \to \infty$. As a result, the states of the system (24) asymptotically converge to the desired fixed point x_d as $t \to \infty$.

Proof. Consider the Lyapunov function candidate V such that

$$
V = \frac{1}{2}a_1\xi_1^2 + \frac{1}{2}a_2\xi_2^2 + \frac{1}{2}a_3\xi_3^2 + \frac{1}{2}a_4\xi_4^2 + \frac{1}{2}a_5\xi_5^2 + \frac{1}{2}a_6\xi_6^2 + \frac{1}{2}a_7\xi_7^2 + \frac{1}{2}a_8\xi_8^2 + \frac{1}{2}a_9\xi_9^2. \tag{31}
$$

The derivative of V with respect to time is

$$
\dot{V} = a_1\xi_1\dot{\xi}_1 + a_2\xi_2\dot{\xi}_2 + a_3\xi_3\dot{\xi}_3 + a_4\xi_4\dot{\xi}_4 + a_5\xi_5\dot{\xi}_5 + a_6\xi_6\dot{\xi}_6 + a_7\xi_7\dot{\xi}_7 + a_8\xi_8\dot{\xi}_8 + a_9\xi_9\dot{\xi}_9. \tag{32}
$$

Using the model of the error system given by (27), and applying the control law given by (30) and the constraints on the parameters a_2, a_4, a_7, a_8 and a_9 given by (29) in the derivative of V given by (32), we obtain:

$$
\begin{aligned}
\dot{V} = &-(2+c_1)a_1\xi_1^2 - 9a_2\xi_2^2 - (4+c_2)a_3\xi_3^2 - 5a_4\xi_4^2 - (1+c_3)a_5\xi_5^2 - (1+c_4)a_6\xi_6^2 \\
&- 5a_7\xi_7^2 - 10a_8\xi_8^2 - 5a_9\xi_9^2.
\end{aligned} \tag{33}
$$

Since the design parameters a_i, for $i = 1, \ldots, 9$, and c_i, for $i = 1, \ldots, 4$, are positive constants, it follows that $\dot{V}$ is negative definite. Also, $\lim_{\|\xi\|\to\infty} V = \infty$. Hence, V is radially unbounded. Here $\xi = [\xi_1, \ldots, \xi_9]^T$.

Given that the Lyapunov function V in (31) is positive definite and radially unbounded, and its derivative w.r.t to to the trajectories in (27) is negative definite, we conclude that the error $\xi_i(t)$, for $i = 1, \ldots, 9$, defined in (26), converge asymptotically to zero as $t \to \infty$. Consequently, the states of the controlled system converge asymptotically to the desired constant fixed point x_d as $t \to \infty$. □

A.2 *Controller design for driving the dynamics of the reduced-order model to periodic orbits or chaotic states*

In this section, we a design Lyapunov-based controller to regulate the dynamics of the reduced-order model toward periodic or chaotic states. The proposed approach involves synchronizing two ODE systems derived from the two-dimensional Navier-Stokes equations using a truncated Fourier expansion, with either identical or different Reynolds numbers. We first derive the error system between the two ODE systems: the master system (the first ODE system) and the slave system (the second ODE system) to be synchronized.

The model of the first ODE system is as follows

$$
\begin{aligned}
\dot{x}_1 &= -2x_1 + 4x_2x_7 - 3\sqrt{2}x_3x_8 - 4x_4x_5,\\
\dot{x}_2 &= -9x_2 + 3x_1x_7 + 9x_6x_8,\\
\dot{x}_3 &= -4x_3 + 4\sqrt{2}x_1x_8 + 4\sqrt{2}x_6x_7 - 4\sqrt{2}x_4x_6 + 8R_{e_1},\\
\dot{x}_4 &= -5x_4 + x_1x_5 + 3\sqrt{2}x_3x_6 - \frac{9\sqrt{5}}{5}x_5x_8,\\
\dot{x}_5 &= -x_5 + 3x_1x_4 - \sqrt{5}x_1x_6 + \sqrt{5}x_4x_8,\\
\dot{x}_6 &= -x_6 + \sqrt{5}x_1x_5 - x_2x_8 + \sqrt{2}x_3x_4 - \sqrt{2}x_3x_7,\\
\dot{x}_7 &= -5x_7 - 7x_1x_2 - \frac{9\sqrt{5}}{5}x_1x_9 - 3\sqrt{2}x_3x_6,\\
\dot{x}_8 &= -10x_8 - \sqrt{2}x_1x_3 - 8x_2x_6 + \frac{4\sqrt{5}}{5}x_4x_5,\\
\dot{x}_9 &= -5x_9 + \frac{9\sqrt{5}}{5}x_1x_7.
\end{aligned}
\tag{34}
$$

Where R_{e_1} is the Reynolds number of the first ODE system. The model of the second ODE system is

$$
\begin{aligned}
\dot{y}_1 &= -2y_1 + 4y_2y_7 - 3\sqrt{2}y_3y_8 - 4y_4y_5 + u_1,\\
\dot{y}_2 &= -9y_2 + 3y_1y_7 + 9y_6y_8,\\
\dot{y}_3 &= -4y_3 + 4\sqrt{2}y_1y_8 + 4\sqrt{2}y_6y_7 - 4\sqrt{2}y_4y_6 + 8R_{e_2} + u_2,
\end{aligned}
$$

$$
\begin{aligned}
\dot{y}_4 &= -5y_4 + y_1y_5 + 3\sqrt{2}y_3y_6 - \frac{9\sqrt{5}}{5}y_5y_8,\\
\dot{y}_5 &= -y_5 + 3y_1y_4 - \sqrt{5}y_1y_6 + \sqrt{5}y_4y_8 + u_3,\\
\dot{y}_6 &= -y_6 + \sqrt{5}y_1y_5 - y_2y_8 + \sqrt{2}y_3y_4 - \sqrt{2}y_3y_7 + u_4,\\
\dot{y}_7 &= -5y_7 - 7y_1y_2 - \frac{9\sqrt{5}}{5}y_1y_9 - 3\sqrt{2}y_3y_6,\\
\dot{y}_8 &= -10y_8 - \sqrt{2}y_1y_3 - 8y_2y_6 + \frac{4\sqrt{5}}{5}y_4y_5,\\
\dot{y}_9 &= -5y_9 + \frac{9\sqrt{5}}{5}y_1y_7.
\end{aligned}
\tag{35}
$$

Where $y_i(i = 1, ..., 9)$ are the state variables of the second ODE and R_{e_2} is its Reynolds number.

Note the addition of controllers $u_1, \ldots, u_4$ in the dynamic model of the slave system. These controllers will be designed to force the states of the slave system to follow the states of the master system.

Define the errors $\xi_i(i = 1, ..., 9)$ as follows:

$$
\begin{aligned}
\xi_1 &= x_1 - y_1,\\
\xi_2 &= x_2 - y_2,\\
\xi_3 &= x_3 - y_3,\\
\xi_4 &= x_4 - y_4,\\
\xi_5 &= x_5 - y_5,\\
\xi_6 &= x_6 - y_6,\\
\xi_7 &= x_7 - y_7,\\
\xi_8 &= x_8 - y_8,\\
\xi_9 &= x_9 - y_9.
\end{aligned}
\tag{36}
$$

Using equations (34)-(36), we obtain the model of the error system as follows :

$$
\begin{aligned}
\dot{\xi}_1 =& -2\xi_1 - 4\xi_4\xi_5 - 4y_5\xi_4 - 4y_4\xi_5 + 4\xi_2\xi_7 + 4y_7\xi_2 + 4y_2\xi_7 \\
& - 3\sqrt{2}\xi_3\xi_8 - 3\sqrt{2}y_8\xi_3 - 3\sqrt{2}y_3\xi_8 - u_1, \\
\dot{\xi}_2 =& -9\xi_2 + 3\xi_1\xi_7 + 3y_7\xi_1 + 3y_1\xi_7 + 9\xi_6\xi_8 + 9y_8\xi_6 + 9y_6\xi_8, \\
\dot{\xi}_3 =& -4\xi_3 + 4\sqrt{2}\xi_1\xi_8 + 4\sqrt{2}y_8\xi_1 + 4\sqrt{2}y_1\xi_8 + 4\sqrt{2}\xi_6\xi_7 + 4\sqrt{2}y_7\xi_6 + 4\sqrt{2}y_6\xi_7 \\
& - 4\sqrt{2}\xi_4\xi_6 - 4\sqrt{2}y_6\xi_4 - 4\sqrt{2}y_4\xi_6 + 8R - u_2, \\
\dot{\xi}_4 =& -5\xi_4 + \xi_1\xi_5 + y_5\xi_1 + y_1\xi_5 + 3\sqrt{2}\xi_3\xi_6 + 3\sqrt{2}y_6\xi_3 + 3\sqrt{2}y_3\xi_6 \\
& - \frac{9\sqrt{5}}{5}\xi_5\xi_8 - \frac{9\sqrt{5}}{5}y_8\xi_5 - \frac{9\sqrt{5}}{5}y_5\xi_8, \\
\dot{\xi}_5 =& -\xi_5 + 3\xi_1\xi_4 + 3y_4\xi_1 + 3y_1\xi_4 - \sqrt{5}\xi_1\xi_6 - \sqrt{5}y_6\xi_1 - \sqrt{5}y_1\xi_6 \\
& + \sqrt{5}\xi_4\xi_8 + \sqrt{5}y_8\xi_4 + \sqrt{5}y_4\xi_8 - u_3, \\
\dot{\xi}_6 =& -\xi_6 + \sqrt{5}\xi_1\xi_5 + \sqrt{5}y_5\xi_1 + \sqrt{5}y_1\xi_5 - \xi_2\xi_8 - y_8\xi_2 - y_2\xi_8 + \sqrt{2}\xi_3\xi_4 \\
& + \sqrt{2}y_4\xi_3 + \sqrt{2}y_3\xi_4 - \sqrt{2}\xi_3\xi_7 - \sqrt{2}y_7\xi_3 - \sqrt{2}y_3\xi_7 - u_4, \\
\dot{\xi}_7 =& -5\xi_7 - 7\xi_1\xi_2 - 7y_2\xi_1 - 7y_1\xi_2 - \frac{9\sqrt{5}}{5}\xi_1\xi_9 - \frac{9\sqrt{5}}{5}y_9\xi_1 - \frac{9\sqrt{5}}{5}y_1\xi_9 - 3\sqrt{2}\xi_3\xi_6 \\
& - 3\sqrt{2}y_6\xi_3 - 3\sqrt{2}y_3\xi_6, \\
\dot{\xi}_8 =& -10\xi_8 - \sqrt{2}\xi_1\xi_3 - \sqrt{2}y_3\xi_1 - \sqrt{2}y_1\xi_3 - 8\xi_2\xi_6 - 8y_6\xi_2 - 8y_2\xi_6 \\
& + \frac{4\sqrt{5}}{5}\xi_4\xi_5 + \frac{4\sqrt{5}}{5}y_5\xi_4 + \frac{4\sqrt{5}}{5}y_4\xi_5, \\
\dot{\xi}_9 =& -5\xi_9 + \frac{9\sqrt{5}}{5}\xi_1\xi_7 + \frac{9\sqrt{5}}{5}y_7\xi_1 + \frac{9\sqrt{5}}{5}y_1\xi_7.
\end{aligned}
\tag{37}
$$

Where $R = R_{e_1} - R_{e_2}$.

A.2.1 *Lyapunov-based control*

A Lyapunov based controller is designed to derive the states of the system in (35) to converge asymptotically to the states of the system in (34).

Let the gains $g_i i = (1, ..., 4)$ be positive scalars and let the control gains $b_i (i = 1, ..., 9)$ be positive scalars such that

$$\begin{aligned} 3b_2 - 7b_7 &= 0, \\ 9b_2 - 8b_8 &= 0, \\ -9b_4 + 4b_8 &= 0, \\ -b_7 + b_9 &= 0. \end{aligned} \tag{38}$$

Theorem 2 The control law,

$$\begin{aligned} u_1 =& -4\xi_4\xi_5 - 4y_5\xi_4 - 4y_4\xi_5 + 4\xi_2\xi_7 + 4y_7\xi_2 + 4y_2\xi_7 - 3\sqrt{2}\xi_3\xi_8 - 3\sqrt{2}y_8\xi_3 \\ & - 3\sqrt{2}y_3\xi_8 + 3\frac{b_2}{b_1}\xi_2\xi_7 + 3\frac{b_2}{b_1}y_7\xi_2 + \frac{b_4}{b_1}\xi_4\xi_5 + \frac{b_4}{b_1}y_5\xi_4 - 7\frac{b_7}{b_1}\xi_2\xi_7 \\ & - 7\frac{b_7}{b_1}y_2\xi_7 - \frac{9\sqrt{5}}{5}\frac{b_7}{b_1}\xi_7\xi_9 - \frac{9\sqrt{5}}{5}\frac{b_7}{b_1}y_9\xi_7 - \sqrt{2}\frac{b_8}{b_1}\xi_3\xi_8 - \sqrt{2}\frac{b_8}{b_1}y_3\xi_8 \\ & + \frac{9\sqrt{5}}{5}\frac{b_9}{b_1}\xi_7\xi_9 + \frac{9\sqrt{5}}{5}\frac{b_9}{b_1}y_7\xi_9 + g_1\xi_1, \\ u_2 =& 4\sqrt{2}\xi_1\xi_8 + 4\sqrt{2}y_8\xi_1 + 4\sqrt{2}y_1\xi_8 + 4\sqrt{2}\xi_6\xi_7 + 4\sqrt{2}y_7\xi_6 + 4\sqrt{2}y_6\xi_7 \\ & - 4\sqrt{2}\xi_4\xi_6 - 4\sqrt{2}y_6\xi_4 - 4\sqrt{2}y_4\xi_6 + 3\sqrt{2}\frac{b_4}{b_3}\xi_4\xi_6 + 3\sqrt{2}\frac{b_4}{b_3}y_6\xi_4 \\ & - 3\sqrt{2}\frac{b_7}{b_3}\xi_6\xi_7 - 3\sqrt{2}\frac{b_7}{b_3}y_6\xi_7 - \sqrt{2}\frac{b_8}{b_3}y_1\xi_8 + g_2\xi_3 + 8R, \\ u_3 =& 3\xi_1\xi_4 + 3y_4\xi_1 + 3y_1\xi_4 - \sqrt{5}\xi_1\xi_6 - \sqrt{5}y_6\xi_1 - \sqrt{5}y_1\xi_6 \\ & + \sqrt{5}\xi_4\xi_8 + \sqrt{5}y_8\xi_4 + \sqrt{5}y_4\xi_8 + \frac{b_4}{b_5}y_1\xi_4 - \frac{9\sqrt{5}}{5}\frac{b_4}{b_5}\xi_4\xi_8 \\ & - \frac{9\sqrt{5}}{5}\frac{b_4}{b_5}y_8\xi_4 + \frac{4\sqrt{5}}{5}\frac{b_8}{b_5}\xi_4\xi_8 + \frac{4\sqrt{5}}{5}\frac{b_8}{b_5}y_4\xi_8 + g_3\xi_5, \end{aligned}$$

$$
\begin{aligned}
u_4 =& \sqrt{5}\xi_1\xi_5 + \sqrt{5}y_5\xi_1 + \sqrt{5}y_1\xi_5 - \xi_2\xi_8 - y_8\xi_2 - y_2\xi_8 + \sqrt{2}\xi_3\xi_4 \\
&+ \sqrt{2}y_4\xi_3 + \sqrt{2}y_3\xi_4 - \sqrt{2}\xi_3\xi_7 - \sqrt{2}y_7\xi_3 - \sqrt{2}y_3\xi_7 + 9\frac{b_2}{b_6}\xi_2\xi_8 + 9\frac{b_2}{b_6}y_8\xi_2 \\
&+ 3\sqrt{2}\frac{b_4}{b_6}y_3\xi_4 - 3\sqrt{2}\frac{b_7}{b_6}y_3\xi_7 - 8\frac{b_8}{b_6}\xi_2\xi_8 - 8\frac{b_8}{b_6}y_2\xi_8 + g_4\xi_6,
\end{aligned} \tag{39}
$$

when applied to the error system (37), guarantees the convergence of errors $\xi_i (i = 1, \ ..., \ 9)$ to zero as t tends to infinity. Therefore, the states of system (35) converge asymptotically to the states of system (34) as t tends to infinity.

Proof. Consider the Lyapunov function candidate V such that

$$
V = \frac{1}{2}b_1\xi_1^2 + \frac{1}{2}b_2\xi_2^2 + \frac{1}{2}b_3\xi_3^2 + \frac{1}{2}b_4\xi_4^2 + \frac{1}{2}b_5\xi_5^2 + \frac{1}{2}b_6\xi_6^2 + \frac{1}{2}b_7\xi_7^2 + \frac{1}{2}b_8\xi_8^2 + \frac{1}{2}b_9\xi_9^2. \tag{40}
$$

The derivative of V with respect to time is

$$
\dot{V} = b_1\xi_1\dot{\xi}_1 + b_2\xi_2\dot{\xi}_2 + b_3\xi_3\dot{\xi}_3 + b_4\xi_4\dot{\xi}_4 + b_5\xi_5\dot{\xi}_5 + b_6\xi_6\dot{\xi}_6 + b_7\xi_7\dot{\xi}_7 + b_8\xi_8\dot{\xi}_8 + b_9\xi_9\dot{\xi}_9. \tag{41}
$$

Using the model of the error system given by (37) in (41), and applying the control law given by (39), the constraints on the parameters b_2, b_4, b_7, b_8 and b_9 given by (38) we obtain:

$$
\begin{aligned}
\dot{V} =& -2b_1\xi_1^2 - 9b_2\xi_2^2 - 4b_3\xi_3^2 - 5b_4\xi_4^2 - b_5\xi_5^2 - b_6\xi_6^2 - 5b_7\xi_7^2 - 10b_8\xi_8^2 - 5b_9\xi_9^2 - g_1b_1\xi_1^2 \\
&- g_2b_3\xi_3^2 - g_3b_5\xi_5^2 - g_4b_6\xi_6^2.
\end{aligned} \tag{42}
$$

Since the design parameters b_i for $i = 1, \ \ldots, \ 9$ and g_i for $i = 1, \ \ldots, \ 4$ are positive constants, it follows that $\dot{V}$ is negative definite. Therefore, the Lyapunov function V in (40) is positive definite, its time derivative $\dot{V}$ is negative definite, and V is radially unbounded. Hence, the error terms $\xi_i(t)$, $i = 1, \ \ldots, \ 9$, in (36) converge asymptotically to zero as $t \to \infty$. Consequently, the states of system (35) asymptotically converge to those of system (34) as $t \to \infty$. □